REVIEW

Check for updates

Design of polymer–metal nanocatalyst interfaces for the electrochemical CO$_2$ reduction reaction

Xi Mao, [ID] [a] Manthan Sarkar[b] and Jie He [ID] *[ab]

The electrochemical CO$_2$ reduction reaction (eCO$_2$RR) offers a promising strategy for carbon cycling by converting the greenhouse gas CO$_2$ into value-added chemicals or fuels. Metal nanocatalysts are among the most desirable catalysts for facilitating CO$_2$ activation. However, achieving high activity, selectivity, and long-term stability in these nanocatalysts remains challenging. Surface modification with synthetic polymer ligands offers an alternative route to resolve those challenges in the eCO$_2$RR without redesigning nanocatalysts themselves. Most recent studies suggest that polymers not only enhance the structural stability of metal nanocatalysts but also provide an interfacial microenvironment that improves the eCO$_2$RR through multiple mechanisms, including increasing the local CO$_2$ concentration, stabilizing intermediates, and suppressing competitive proton reduction. In this review, we summarize the recent advances in the eCO$_2$RR using metal nanocatalysts modified with polymer ligands, including nanocatalysts with hydrophobic, conductive, ionic and porous polymers. We discuss the mechanistic insights underlying polymer–catalyst interactions, with particular emphasis on how these interactions enhance catalytic performance. Finally, we conclude with key challenges and highlight future perspectives in this field.
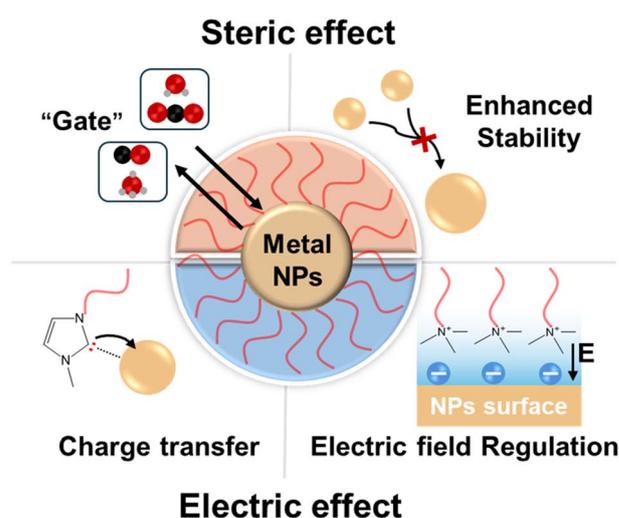
1. Role of surface ligands in catalysis

Metal nanoparticles (NPs) play a central role in heterogeneous catalysis.[1] Due to their ultrasmall dimensions, metal NPs exhibit distinct "nano-effects" (or a high surface-to-volume ratio) that significantly enhance catalytic reactivity relative to their bulk counterparts.[2] Since catalysis primarily occurs at the surface, the overall activity of NPs strongly depends on both surface area and surface energy. These two factors are intrinsically related: increasing surface area exposes more active sites, while the surface energy can be modulated by controlling the exposed crystal facets. Extensive studies and comprehensive reviews have discussed how such surface structures dictate the catalytic performance of metal NPs across a broad range of reactions.[3–7]

Drawing parallels from biological systems, the catalytic efficiency of metalloenzymes is governed by the coordination environment of the metal co-factor, which is defined by both the immediate ligands and extended coordination spheres that critically influence metal-site reactivity. Despite not being directly engaged in the catalytic cycle, these protein frameworks provide a microenvironment for the metal center, affecting local hydrophobicity, dielectric constant, and accessibility of specific reactants.[8] This review seeks to summarize how ligands,

particularly polymer ligands (see Section 2), attached to metal NP surfaces can similarly modulate catalytic performance, as electronic and steric regulators. Numerous studies have reported "positive" ligand effects, where the presence of surface ligands enhances catalytic activity, even though these ligands often rearrange or exchange under reaction conditions. Much like the protein shell of an enzyme, these ligands influence

Scheme 1 Illustrating the role of surface ligands in catalysis mediated by metal NPs.

[a]Polymer Program, Institute of Materials Science, University of Connecticut, Storrs, Connecticut 06269, USA. E-mail: jie.he@uconn.edu

[b]Department of Chemistry, University of Connecticut, Storrs, Connecticut 06269, USA

11848 | *J. Mater. Chem. A*, 2026, **14**, 11848–11879

This journal is © The Royal Society of Chemistry 2026

catalysis by selectively facilitating substrate binding, stabilizing key intermediates, and directing product selectivity.[9–13]

In general, surface ligands on NPs play two principal roles (Scheme 1).[14–17] First, they act as molecular gates, regulating access to the catalytic surface.[15–17] In contrast to the uniform metal centers in homogeneous complexes, surface atoms on NPs display heterogeneous reactivity; atoms located at corners and edges are generally more active than those on flat terraces.[3] Ligand coverage typically forms monolayers on specific facets (e.g., packing on lateral facets), which may reduce substrate adsorption on those regions and increase accessibility on other sites. In the case of polyhedral NPs, this selective exposure can suppress certain adsorption geometries (e.g., thiols on Pd to block the bridge site)[18–20] and consequently alter reaction selectivity. The "gate" effect can also extend beyond steric blockage to include modulation of the interfacial microenvironment, through hydrophobicity, hydrogen bonding, or solvation, thereby influencing how substrates approach and transform at the catalytic surface.[9–12] Second, surface ligands can modify the electronic nature of surface atoms, similar to how donor–acceptor ligands tune transition-metal complexes in homogeneous systems.[21–23] Ligands with comparable steric effects but distinct binding motifs can yield markedly different catalytic outcomes by modifying local charge density (or the d band state of the metal site).[24] Taking Pt supported on carbon (broadly used in organic synthesis for hydrogenation) as an example, interfacial electronic effects induced by ethylenediamine significantly modulate the hydrogenation of nitroaromatics, achieving nearly 100% selectivity for N-hydroxylanilines compared to only 33% with commercial Pt black.[25] The elevated surface electron density effectively stabilizes electron-deficient intermediates, thereby altering the hydrogenation selectivity. Overall, surface ligands can provide an alternative, post-synthetic approach for optimizing the catalytic behavior of metal NPs without re-synthesizing NPs.

2. Surface ligands in the electrochemical CO_2 reduction reaction (eCO_2RR)

The conversion of carbon dioxide (CO_2) into value-added chemicals has attracted considerable attention because it effectively promotes carbon cycling and reduces CO_2 emission.[26,27] CO_2 is thermodynamically stable due to its strong C=O bonds. Therefore, its activation requires substantial energy input and (multiple) electron transfers to overcome thermodynamic and kinetic barriers. To address this challenge, numerous CO_2 conversion strategies have been developed, including photochemical,[28] electrochemical,[29] thermochemical[30] and biochemical[31] reduction pathways. Among these, the electrochemical CO_2 reduction reaction (eCO_2RR) offers a pathway to zero-emission targets potentially by coupling with renewable electricity sources.[32–35] CO_2 has a +4 oxidation state of C and it can be reduced to a spectrum of products, such as CO, formic acid, methane, methanol, ethylene, ethanol and other products.[36–38] Pioneered by Hori et al.,[39] many heterogeneous

catalysts have been studied since the 1980s to activate CO_2 through electroreduction.[40–43] In terms of their activity and selectivity, Group 11 noble metals like Au and Ag are among the most active catalysts for the eCO_2RR. With a low density of reactive d-states, Au and Ag can coordinate CO_2 but have weak binding with *CO, often enabling high selectivity toward CO (>90%).[44–46] Au in the forms of spherical NPs and nanoclusters can reduce CO_2 to CO with overpotentials of 300–450 mV.[47] AuNPs made from the reduction of thick Au oxide films even show an overpotential down to 150 mV as demonstrated by Kanan et al.[45,48–50] p-block metals and their oxides, e.g., Sn and Bi, reduce CO_2 to formate with overpotentials >1 V.[51–53] CO and formic acid that only require two electron transfers are kinetically favorable products and they can be prepared with high selectivity.[54–56] CO also serves as a key intermediate for downstream synthesis coupled with the Fischer–Tropsch process.[57] Cu, on the other hand, has a high d band center and moderate binding affinity with *CO. It is the only catalyst capable of producing C2 or hydrocarbon products,[58] known to be more value-added compared to C1 products, although it is not selective.

In all cases, the hydrogen evolution reactions (HER) compete with the eCO_2RR because of their similar thermodynamic and kinetic barriers.[59] For commercial Cu foil, the HER reaches >50% faradaic efficiency (FE, the percentage of electrons used towards a particular product).[60] To enhance eCO_2RR selectivity, suppressing the HER is essential.[61] Controlling the structure and composition of nanocatalysts has been extensively used in the past to modulate their reactivity.[3,58,62–65] For AuNPs, nanocubes with (100) dominated surface facets show a CO FE close to 94%, while octahedra with (111) facets have a CO FE of about 50%.[66] Similarly, Cu (100) bound CO at a high coverage favors C–C coupling.[67] However, metal nanocatalysts are unstable at reductive potentials and irreversible structure dynamics pose challenges for their long-term applications. Alivisatos's group studied the morphological evolution of CuNPs during the eCO_2RR.[68] 7 nm Cu spherical NPs grew into 23 nm after 10 min electrolysis at −1.25 V vs. the reversible hydrogen electrode (RHE, the same hereafter unless otherwise noted). Similar results were reported by Yang's and Buonsanti's groups.[69,70] Buonsanti's group proposed the underlying mechanisms involved in the structural transformation of Cu-based nanocatalysts during the eCO_2RR, including detachment, dissolution, Ostwald ripening, reshaping, fragmentation, agglomeration and poisoning.[70]

Surface modification has emerged as an effective strategy to address these unmet challenges of nanocatalysts in the eCO_2RR, although ligands have been overlooked as a catalytic barrier.[11,71–73] Recent results have recognized that surface ligands can enhance stability of nanocatalysts, provide selective binding, enhance the local concentration of CO_2, and suppress the competing HER.[74–77] Polymer ligands, with extended chain length, can effectively modulate the catalyst–electrolyte interface as an essential microenvironment to provide CO_2 capture, collectively improving CO_2 binding, the intermediate evolution and the product desorption.[78–80] For example, incorporating FeNPs in porous ZIF-8 for the eCO_2RR allows the porous layers

This journal is © The Royal Society of Chemistry 2026

J. Mater. Chem. A, 2026, 14, 11848–11879 | 11849

to provide a hydrophobic environment for CO_2 adsorption and suppress the HER, thereby achieving 90% CO FE.[81] Positively charged ligands can improve stability of intermediates during electrocatalytic cycles. Aminothiolate-coated Cu for the eCO_2RR can promote initial CO_2 activation by the interaction between the amine group and $*CO_2$.[82] The amine group on the ligands can stabilize *COOH, as the intermediate from the first electron/proton transfer, through hydrogen bonding. As an extended coordination sphere, polymer ligands can also change the mass transport behaviors of ions, water and CO_2. In addition, polymers can present multiple binding motifs that strongly coordinate with metal NPs as compared to small molecular ligands, thereby preventing interparticle sintering

under reaction conditions. For example, polymers having multiple N-heterocyclic carbene (NHC) moieties can significantly improve long-term stability of AuNPs[83,84] with an enhanced CO_2 selectivity.[85] Therefore, polymer ligands on catalysts show advantages in preventing the aggregation of catalysts in addition to modulating the electronic and steric structure.[76,77]

Electronic effects and hydrophobic effects as the two main mechanisms work synergistically to enhance eCO_2RR performance. Electronic effects mainly arise from the binding motifs that dictate the charge perturbation between the ligand and NP surface. The coordination of electron-donating or electron-withdrawing groups can also modify the d-band center of
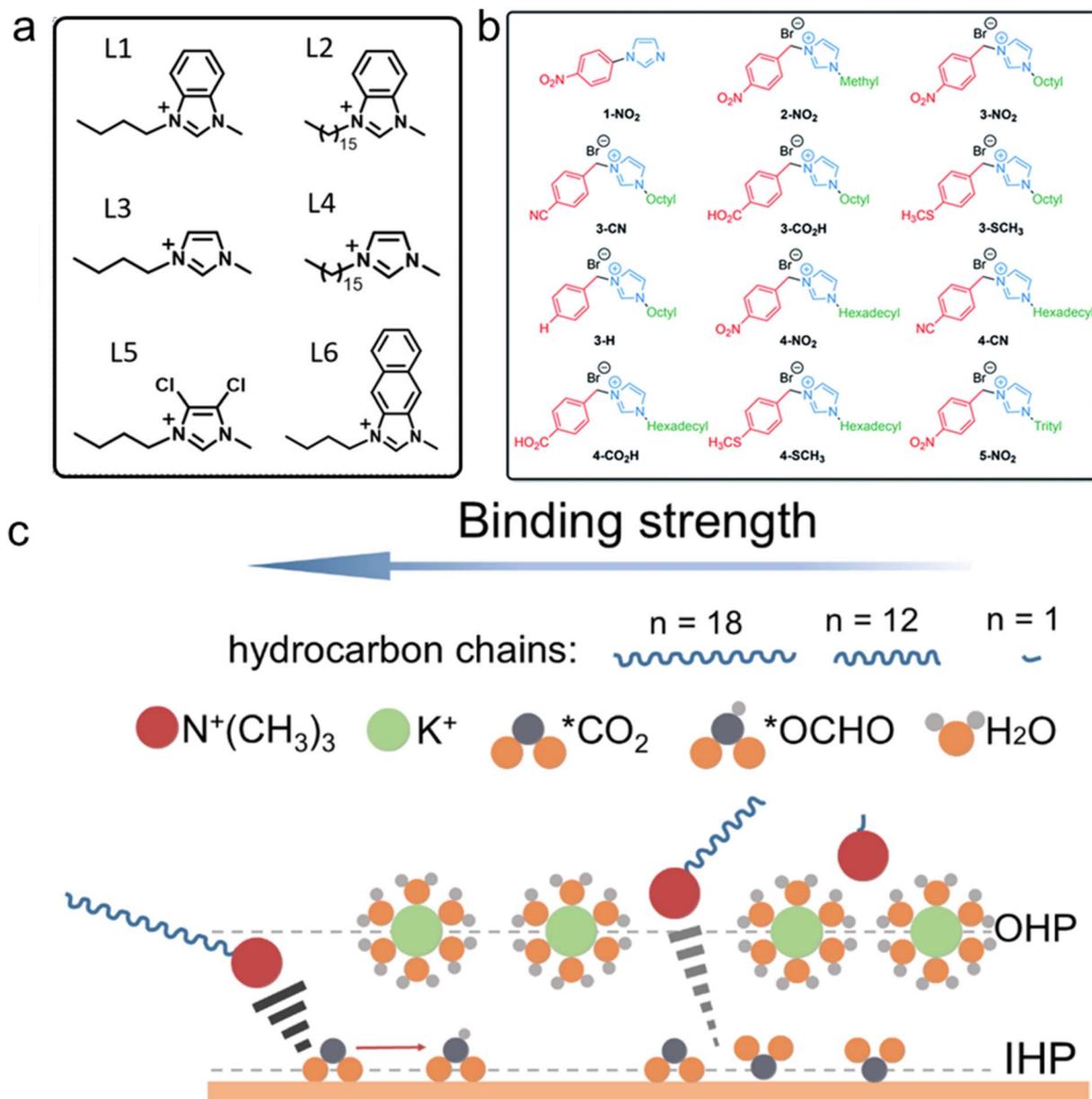

Fig. 1 (a) Chemical structures of NHC ligands. Reproduced with permission.[86] Copyright 2025 American Chemical Society. (b) Chemical structures of imidazolium ligands with tunable anchor and tail groups. Reproduced with permission.[87] Copyright 2019 The Royal Society of Chemistry. (c) Schematic illustrating the steric effect of C_nTA^+ cations with varying backbone lengths on modulating the binding strength of the intermediates. Reproduced with permission.[88] Copyright 2025 Wiley.

11850 | J. Mater. Chem. A, 2026, 14, 11848–11879

This journal is © The Royal Society of Chemistry 2026

NPs, thereby influencing the affinity and stabilization of reactants and intermediates. Electron-donating ligands, such as amines and NHCs, have proven to facilitate the activation of electron-deficient species including CO_2,[86,89] although the underlying mechanisms remain debated. For instance, in molecular NHC–Mn(I) complexes, CO_2 activation may proceed through different pathways: CO_2 can form adducts with the NHC,[90] or alternatively, the NHC can stabilize the formate (*COOH) intermediate via hydrogen bonding, which is generated after the first electron/proton transfer.[91] Our group has investigated the effects of NHC ligands on the eCO_2RR using various NHCs with different electron-donating or -withdrawing group modified gold NPs as catalysts (Fig. 1a).[86] Compared with pure Au/C, NHC (L1) modified Au/C showed ∼33% enhancement in partial current density for CO (J_{CO}), attributed to stabilization of *CO intermediates as confirmed by a shift of *CO vibrational frequency. However, the electronic nature of NHC ligands had a limited effect on the eCO_2RR performance, and AuNPs with NHCs having electron-donating or -withdrawing groups showed similar reactivity for CO_2. Buonsanti and co-workers studied a family of imidazolium ligands with different functional groups and tail groups to promote the eCO_2RR (Fig. 1b).[87] For oleylamine-modified silver nanocrystals (AgNCs), the H_2 FE is ∼70% and CO FE is 29%. After modifying AgNCs with imidazole or imidazolium, the CO_2 selectivity dramatically improved. For example, the CO FE with imidazolium having a p-NO_2 benzyl group (3-NO_2, Fig. 1b) increases to 92%. Additionally, imidazoliums with other electron-withdrawing groups, e.g., CN, CO_2H and SCH_3 benzyl groups, all yielded much lower selectivity (CO FE of 77%). In the absence of electron-withdrawing groups on the p-NO_2 benzyl group, the CO FE with 3-H (Fig. 1b) was as low as 58%.[87]

Hydrophobicity from the extended coordination sphere, although not directly involved in catalysis, can vary the microenvironment for the eCO_2RR.[92] Hydrophobic polymers create a nonpolar interfacial layer (e.g., a few to tens of nanometers) that influences the local distribution of reactants, intermediates, and solvation near the catalyst surface. The eCO_2RR performance is often limited by the low solubility of CO_2 in the aqueous electrolyte in a typical H-cell. The limiting current density (j_{lim}) in the eCO_2RR is proportional to the available CO_2 concentration. The local CO_2 concentration can be described using the surface adsorbed *CO_2 (θ_{CO_2}) as follows: $\theta_{CO_2} = \theta^* \times C_0 \exp(-E_{CO_2}/RT)$, where θ^* is the coverage of available surface sites, C_0 is the local CO_2 concentration, E_{CO_2} is the adsorption energy of CO_2 on the catalyst, R is the ideal gas constant, and T is the temperature.[93,94] By enriching the CO_2 concentration at the catalytic interface, hydrophobic coatings can effectively improve selectivity while confining water molecules and protons. For example, Peters et al. coated an Ag electrode with hydrophobic pyridinium-based additives, which highly suppressed the HER and achieved CO FE >99% due to the slow diffusion of protons through the hydrophobic layer.[95] Moreover, hydrophobicity also modulated the diffusion behavior of ions and gases, forming a confined reaction zone that favors multielectron transfer processes. The degree of hydrophobicity is often tunable through alkyl chain length,[96,97] tail group

structure, or polymer backbone design.[96,97] It determines how strongly the interfacial environment deviates from bulk electrolyte conditions. Sargent and co-workers utilized alkane–thiol modified copper nanoparticles (CuNPs) as catalysts.[97] Compared with pure CuNPs, the alkane–thiol modified CuNPs with chain lengths from C_2 to C_{22} yield a higher FE of acetate. After optimizing the loading, coverage and chain length, the acetate FE reached 70% at 400 mA cm^{-2}. Density functional theory (DFT) calculations indicate that the ethylene intermediate (HOHC–CH_2O)* is more stable than the acetate intermediate (HOOC–CH_2)*; thus acetate is the main product. On the other hand, metal catalysts with intrinsic hydrophobicity that originates from their microstructures showed a high selectivity for CO_2 reduction. Yamauchi and co-workers coated Cu nanoneedle arrays with 1-ocatadecylthiol and obtained a superhydrophobic catalyst layer (water contact angle (WCA): 158.5°), achieving an (C_{2+}) FE of 87% at −1.6 A cm^{-2} under acidic conditions.[98] Inspired by the hydrophobic structure of Setaria, Gao et al. developed a Cu needle array, which exhibited superhydrophobicity with a WCA of 154°. The hydrophobic microstructure trapped a gas layer and enriched the local CO_2 concentration, enabling a high C_{2+} production rate of 255 mA cm^{-2} with a 64% FE.[98–100]

Compared with hydrophobic alkane–thiol ligands, hydrophobic ionic ligands, particularly quaternary ammonium cations (C_nTA^+), can promote the eCO_2RR performance by (i) stabilizing intermediates and repelling protons and (ii) enhancing the mass transport of CO_2 (Fig. 1c).[88] After introducing octadecyl trimethyl ammonium chloride ($C_{18}TAC$) on CuNPs, the FE formate increased to ∼70%, reaching a maximum of 90% at −0.8 V. For pure CuNPs, H_2 is the primary product (∼55% at −0.8 V). The FE formate increases with the increase of alkyl chain length. The FE formate of $C_{18}TAC$ modified CuNPs is 72.2% that is 2.0 and 2.9 times higher than those of $C_{12}TAC$ and C_1TAC modified-CuNPs, respectively. The local hydrophobicity is therefore crucial in suppressing the HER and promoting selectivity to CO_2 during the eCO_2RR. Other than ammonium, benzimidazolium is another attractive ionic ligand that enhances eCO_2RR performance by modifying the interfacial electric field and buffering local pH in strongly acidic environments, achieving 80% (C_{2+}) FE at 100 mA cm^{-2}. The simulation results indicate that the surface electric field enables CO_2 activation in acidic media. Meanwhile, replacing alkali metal cations with benzimidazolium enhances the stability for over 150 h.[101]

Polymer ligands are fundamentally different from molecular ligands. Molecular ligands often form self-assembled monolayers (SAMs) on NPs. SAMs are typically dense and electronically insulating, thereby known as charge and ion insulators.[102–106] On flat Au electrodes as an example, the SAMs of organothiols with long alkyl chains can block the access of redox species to the electrode.[102,103] The presence of pinhole defects, e.g., shorter alkyl chains[65] or less flat surfaces,[107] allows the permeation of ionic species. As a result, NPs with polyhedral surfaces potentially bring more pinhole defects at the edge and corner sites where the redox species have access to the NP surface, compared to the flat metal electrode. On the other

This journal is © The Royal Society of Chemistry 2026

J. Mater. Chem. A, 2026, 14, 11848–11879 | 11851

hand, polymer ligands, due to their large steric effect, do not form a dense layer, particularly through the "grafting to" approach. Typically, the grafting density of molecular thiols is about 3–9 nm^{-2},[108] while it is 0.1–0.5 nm^{-2} for polymers.[109,110] Their long chains therefore form a semi-permeable shell that allows the diffusion of small molecules/ions and reaction intermediates (Fig. 2a). Our group has measured the interfacial mass transfer kinetics using three molecular redox probes, *i.e.*, ferricyanide, ruthenium hexaammine and ferrocenecarboxylic acid.[111] With molecular NHCs that form compact SAMs (Fig. 2b and c), there is a dramatic decrease in redox current and the apparent diffusion coefficient (D_0). In the case of ruthenium hexaammine, D_0 dropped about three orders of magnitude, suggesting slow ion transport limited to low-density pinhole defects within the SAM. In contrast, polymeric NHC ligands had a minor impact on D_0, and, in some cases, the increase in D_0 was observed for more hydrophobic probes, *e.g.*, ferrocene-carboxylic acid. These results suggest that polymer ligands form a permeable interface for both small ions and larger redox probes (Fig. 2d). Consequently, in the eCO$_2$RR, where proton-coupled electron transfer dominates, hydrophobic polymer NHCs are unlikely to prevent the diffusion of hydrated ions.

As discussed above, surface ligand modification plays a critical role in the eCO$_2$RR and offers a promising way to tune the surface microenvironment of nanocatalysts. There are excellent reviews on the effects of binders on the eCO$_2$RR,[112] ligand impact on heterogeneous electrocatalysis,[77] and ligand-modified catalysts for the eCO$_2$RR.[76,80] None of these reviews specifically address using polymer-modified nanocatalysts as a strategy for enhancing eCO$_2$RR performance. In the current review, we summarized the recent progress in polymer-modified metal nanocatalysts for the eCO$_2$RR. We categorized polymer ligands into four types based on their functions: (i) hydrophobic polymers, which control the mass transfer of CO$_2$ and the hydrogen bonding network of water; (ii) conductive polymers, which balance the conductivity and hydrophobicity; (iii) ionic polymers, which stabilize the intermediates and vary the localized ion concentration, while synergistically hydrophobic polymer backbones improve CO$_2$ reduction performance; and (iv) porous polymers, including metal–organic frameworks (MOFs) and covalent–organic frameworks (COFs), both of which offer high surface area and great potential to capture CO$_2$. We highlight the current status and challenges in this rapidly evolving field. Continued progress in this area will not only deepen the mechanistic understanding of ligand effects in electrocatalysis but also accelerate the rational design of next-generation hybrid nanocatalysts for efficient and selective CO$_2$ conversion.

3. Hydrophobic polymer ligands for the eCO$_2$RR

Nanocatalysts with suitable surface hydrophobicity can significantly regulate the product distribution of the eCO$_2$RR. One effective strategy to adjust this hydrophobicity is the introduction of ligands. It is well-known that organothiols containing
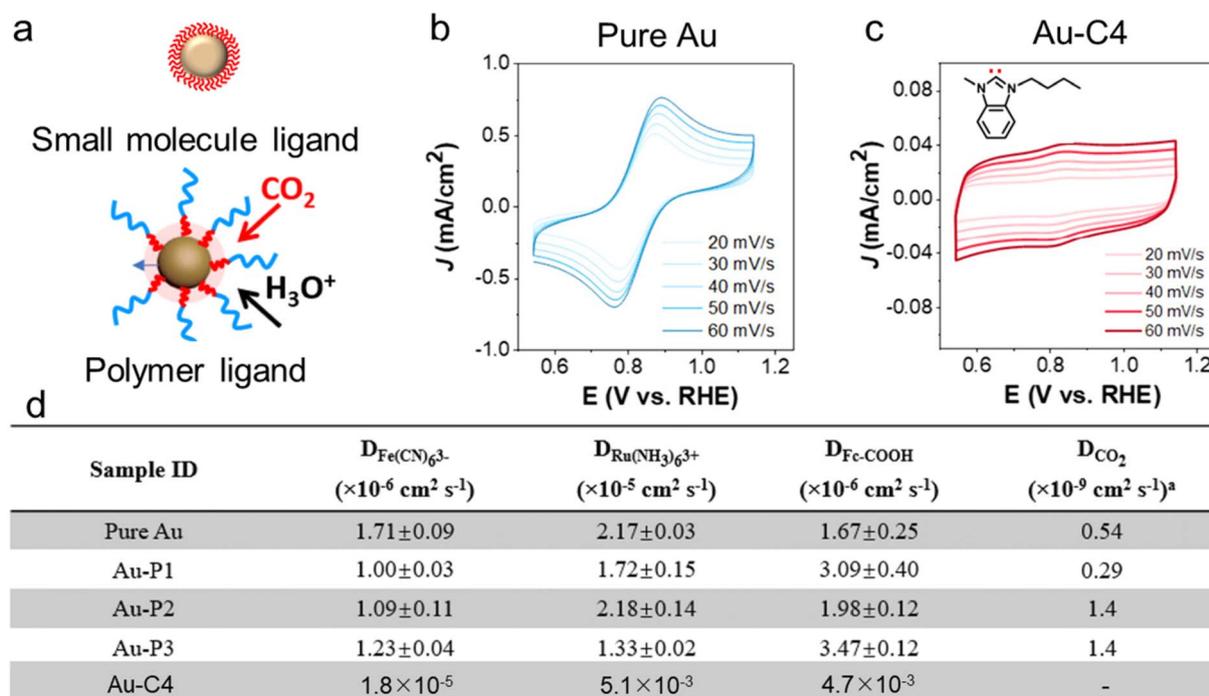

Sample ID	$D_{Fe(CN)_6^{3-}}$ ($\times10^{-6}$ cm^2 s^{-1})	$D_{Ru(NH_3)_6^{3+}}$ ($\times10^{-5}$ cm^2 s^{-1})	$D_{Fc\text{-}COOH}$ ($\times10^{-6}$ cm^2 s^{-1})	D_{CO_2} ($\times10^{-9}$ cm^2 s^{-1})^a
Pure Au	1.71±0.09	2.17±0.03	1.67±0.25	0.54
Au-P1	1.00±0.03	1.72±0.15	3.09±0.40	0.29
Au-P2	1.09±0.11	2.18±0.14	1.98±0.12	1.4
Au-P3	1.23±0.04	1.33±0.02	3.47±0.12	1.4
Au-C4	1.8×10^{-5}	5.1×10^{-3}	4.7×10^{-3}	-

Fig. 2 (a) Schematic illustration of small molecule and polymer ligand modified metal nanocatalysts for CO$_2$ and proton transport. Cyclic voltammetry scans of (b) AuNPs and (c) Au–C4 measured with 5 mM K$_3$Fe(CN)$_6$ at various scan rates. Reproduced with permission.[86] Copyright 2025 American Chemical Society. (d) Summary of the diffusion coefficient (D) using various probe molecules including Fe(CN)$_6^{3-}$, Ru(NH$_3$)$_6^{3+}$, Fc–COOH, and CO$_2$. P1–P3: *N*-heterocyclic carbene (NHC)-functionalized poly(ethylene oxide) (NHC–PEO·HCO$_3^-$, P1), NHC–PS·HCO$_3^-$ (P2), and block copolymer NHC–PEO-*b*-PS·HCO$_3^-$ (P3). Reproduced with permission.[111] Copyright 2023 The Royal Society of Chemistry.

11852 | *J. Mater. Chem. A*, 2026, **14**, 11848–11879

This journal is © The Royal Society of Chemistry 2026

Table 1 Summary of polymer–metal hybrid nanocatalysts and their eCO$_2$RR performance

Polymer types	Advantages	Disadvantages	Materials	Water contact angle	Main product	FE$_{product}$ (%)	FE$_{H_2}$ (%)	$J_{product}^a$ (mA cm^{-2})	E^b (V)	Electrolyte	Cell type	Stability	Ref.
Hydrophobic polymers	Increasing local CO$_2$ concentration	Poor conductivity	AuNPs/PVBMB-Im·HCO$_3^-$	—	CO	90	~10	—	−0.9	0.1 M KHCO$_3$	H-cell	11 h	85
			AuNPs/NHC–PS·HCO$_3^-$	—	CO	~90	~10	21.2	−0.9	0.1 M KHCO$_3$	H-cell	1 h	111
			AuNPs/PTFE	—	CO	94.7	~5	—	−0.7	0.25 M Na$_2$CO$_3$	H-cell	3 h	120
			CuNPs/PTFE	145°	C$_{2+}$	95.4	~5	—	−1.6	1 M KOH	Flow cell	12 h	121
	Suppressing the HER	Slowing down proton transfer	CuNWs/AuNWs/NHC–PS·HCO$_3^-$	—	C$_{2+}$	65	20	120	−1.1	0.5 M KHCO$_3$	Flow cell	12 h	130
			CuO/FEP	144°	C$_{2+}$	52	22	37.4	−1.1	0.1 M KHCO$_3$	H-cell	—	132
						62	8	220	−0.71	1 M KOH	Flow cell	16 h	132
	Enhancing nanocatalysts' stability		CuO/PAA	32°	C$_{2+}$	35	32	18	−1.1	0.1 M KHCO$_3$	H-cell	—	132
						35	38	87.6	−0.71	1 M KOH	Flow cell	—	132
			CuO/Nafion	132°	C$_{2+}$	45	40	25	−1.1	0.1 M KHCO$_3$	H-cell	—	132
						50	15	150	−0.71	1 M KOH	Flow cell	—	132
Conductive polymers	Improving electron transfer	Complex synthesis	CuNSs/PANI	—	C$_2$H$_4$	58	~38	30.2	−1.2	0.1 M KCl	H-cell	10 h	134
			CuNPs/ABSA–PANI	142°	C$_{2+}$	81	~10	487	−2.6	1 M KCl (pH = 1)	Flow cell	11 h	135
	Enhancing CO$_2$ concentration	Poor adhesion and processing	CuPEDOT	—	CH$_4$	62.7	~6	354	−1.58	1 M KOH	Flow cell	15 h	136
	Suppressing the HER		PPy@HKUST-1	—	CH$_4$	56	18	140	−0.8	1 M KOH	Flow cell	20 h	140
			PANI@HKUST-1	—	C$_2$H$_4$	67.5	12	410	−0.9	1 M KOH	Flow cell	20 h	140
Ionic polymers	Enhancing CO$_2$ solubility	Complex synthesis	CoTAPc/PFBr	69°	CO	98.6	—	22.5	−1.1	0.5 M KHCO$_3$	H-cell	5 h	141
			CuNPs/PFSA/SSCD72	127°	C$_{2+}$	32	20		−1.1	0.1 M KHCO$_3$	H-cell	—	147
	Adjusting CO$_2$/proton mass transfer	Poor conductivity	CuNPs/PFSA/SSCD79	134°	C$_{2+}$	34	16		−1.1	0.1 M KHCO$_3$	H-cell	—	147
			CuNPs/PFSA/LSCD520	142°	C$_{2+}$	44	10		−1.1	0.1 M KHCO$_3$	H-cell	—	147
			CuNPs/PFSA/LSCD521	146°	C$_{2+}$	32	8		−1.1	0.1 M KHCO$_3$	H-cell	—	147
	Suppressing the HER		CuNPs/PSImC$_{16}$	~100°	CO	80	5	109	−1.2	0.5 M KHCO$_3$	H-cell	9 h	148
			AuNPs/PS–quaternary ammonium	—	CO	94	6	41	−1.5	0.1 M KHCO$_3$	H-cell	15 h	153
	Stabilizing intermediates		CuNPs/pTPN–TMA	81°	C$_2$H$_4$	21	42.5	—	−1.2	0.1 M KHCO$_3$	H-cell	—	154
			CuNPs/pTPN–Pip	79°	C$_2$H$_4$	8.7	52	—	−1.2	0.1 M KHCO$_3$	H-cell	—	154
			CuNPs/pTPN–Py	82°	C$_2$H$_4$	14	42	—	−1.2	0.1 M KHCO$_3$	H-cell	—	154
			CuNPs/pTPN–Meim	67°	CH$_4$	9	74	—	−1.2	0.1 M KHCO$_3$	H-cell	—	154

This journal is © The Royal Society of Chemistry 2026

J. Mater. Chem. A, 2026, 14, 11848–11879 | 11853

Table 1 (Contd.)

Polymer types	Advantages	Disadvantages	Materials	Water contact angle	Main product	$FE_{product}$ (%)	FE_{H_2} (%)	$J_{product}^a$ (mA cm^{-2})	E^b (V)	Electrolyte	Cell type	Stability	Ref.
			CuNPs/pTPN–Hexim	75°	C$_2$H$_4$	21	55	—	−1.2	0.1 M KHCO$_3$	H-cell	—	154
			CuNPs/pTPN–Beim	88°	C$_2$H$_4$	46	18	331	−1.2	0.1 M KHCO$_3$	H-cell	—	154
			AuNPs/polyzwitterions (P6)	85°	CO	90	8	3.7	−0.8	0.1 M KHCO$_3$	H-cell	—	156
			AuNPs/polyzwitterions (P7)	16°	CO	70	28	—	−0.8	0.1 M KHCO$_3$	H-cell	—	156
			AuNPs/polyzwitterions (P8)	5°	CO	54	44	—	−0.8	0.1 M KHCO$_3$	H-cell	—	156
			InNPs/c-PDDA	143°	HCOO$^-$	75	10	225	−1.6	0.4 M K$_2$SO$_4$ (pH = 1)	Flow cell	36 h	157
			Cu@PIL	129°	CH$_4$	42	16	111	−0.95	1 M KOH	Flow cell	24 h	158
Porous polymers	Improving CO$_2$ concentration	Slowing down proton transfer	Cu$_2$ONPs/MOF	—	CH$_3$CH$_2$OH	44	20	9.7	−0.6	0.5 M KHCO$_3$	H-cell	47 h	184
	Suppressing the HER	Poor conductivity	CuNCs/MOF	—	C$_2$H$_4$	50	16	—	−1.2	0.1 M KHCO$_3$	H-cell	8 h	185
			2Bn–Cu@UiO-67	—	CH$_4$	81	~5	420	−1.5	0.5 M KHCO$_3$	Flow cell	2 h	188
			Cu$_2$O@CuHTTP	—	CH$_4$	73	22	10.8	−1.4	0.1 M KCl/0.1 M KHCO$_3$	H-cell	—	190
	Stabilizing intermediates		Cu/CeO$_2$/C	—	CH$_4$	80	10	139	−1.5	0.5 M KHCO$_3$	Flow cell	9 h	211
			AuNN@PCN	—	C$_2$H$_4$	53	20	—	−1.2	0.1 M KHCO$_3$	H-cell	10 h	213

^{a} $J_{product}$ (mA cm^{-2}): current density of products. ^{b} E (V): applied potentials E (V vs. RHE).

11854 | J. Mater. Chem. A, 2026, 14, 11848–11879

This journal is © The Royal Society of Chemistry 2026

long alkyl chains reduce water wettability of metals.[113–115] Cu dendrites modified with 1-octadecanethiol exhibit superhydrophobic behavior, showing a WCA as high as 153°, as demonstrated by Mougel and co-workers.[116] The altered wettability modifies the electrolyte–electrode interface; with reduced water accessibility, stronger reducing potentials are required to drive CO_2 conversion (as summarized in Table 1). The hydrophilic Cu dendrite without 1-octadecanethiol only needed -0.68 V to reach a current density of -5 mA cm^{-2}, whereas its hydrophobic counterpart required -1.38 V. The hydrophobic Cu dendrites achieved notably improved selectivity, with a ethylene FE of 56% and 17% for ethanol, compared to 9% and 4% for unmodified Cu under neutral conditions. Organothiols can form SAMs on many metal surfaces,[67] including all metals in Group 11, making them ideal for controlling surface hydrophobicity during the eCO$_2$RR. Nevertheless, metal–thiolate binding is not electrochemically stable. For example, cyclic voltammetry or impedance spectroscopy studies suggest that the stability window of Au–thiolate monolayer is 0–1 V.[117] Cu–thiolate is slightly more stable against reduction until -0.6 V.[118] Under reductive conditions for the eCO$_2$RR, the desorption of thiols likely occurs concurrently with or even before the reduction of CO_2.

Daasbjerg's group demonstrated that polymer hydrophobicity impacted the electrode–electrolyte interfaces in water during the eCO$_2$RR on a CuO electrode.[119] With drop casting, hydrophobic poly(vinylidene fluoride) and polyethylene coatings (ca. 0.7–1 μM) enhanced the catalytic efficiency and CO_2 to C_2H_4 selectivity (32%, as compared to 16.7% for CuO at -1.12 V) by suppressing the HER through high surface pH and restricted water diffusion, whereas coating with hydrophilic polymers, such as poly(vinylpyrolidine), increased the HER.

Polytetrafluoroethylene (PTFE), composed of densely fluorinated carbon chains, is a classic example of a highly hydrophobic polymer widely utilized to tailor electrode surfaces in the eCO$_2$RR.[120–122] Its chemical inertness against redox reactions, low surface energy, and high crystallinity make it an ideal additive or coating material for improving catalytic performance and selectivity. AuNPs supported on carbon and mixed with PTFE showed a high CO FE of 94.7% at -0.7 V compared to ~88% of poly(vinyl alcohol) (PVA) modified AuNPs.[120] Porous

PTFE nanocoating on CuNPs by physical mixing provided a high surface area for CO_2 transport, and high hydrophobicity increased the retention of CO from PTFE-covered Cu surfaces, achieving an (C$_{2+}$) FE of 78% at 400 mA cm^{-2}.[121] In addition, hydrophobicity could be introduced by simply mixing CuNPs with PTFE, which limited the interface with liquid electrolyte and enhanced the local CO_2 concentration, achieving a 2 times increase in the single-pass conversion rate, in comparison with the electrode without PTFE.[93] Meanwhile, the finite diffusion layer thickness (δ), calculated from the electrochemical impedance spectra (EIS) using the equivalent impedance (Z_d), decreased from 20.2 to 3.2 μm after mixing PTFE with nanocatalysts, indicating improved mass transport and CO_2 adsorption, thereby enhancing the (C$_{2+}$) FE.

N-Heterocyclic carbene (NHC)-functionalized polymers are believed to strengthen ligand coatings through forming covalent-like metal–carbon bonds (50–100 kcal mol^{-1} for group 10 and 11 metals).[123–125] As strong σ-donor ligands, NHCs can effectively modulate the electronic structure of catalytic surfaces. Due to their exceptional binding affinity, NHCs can replace various native capping ligands on metal NPs, including thiols, thioethers, and oleates. However, free NHCs are typically highly reactive and unstable under air or moisture, which limits their direct use for modifying metal NPs synthesized in aqueous environments.

Over the past few years, our group has developed two distinct "grafting-to" strategies for introducing NHC-functionalized polymer ligands onto metal NPs.[126–129] The first approach relies on transmetalation, in which NHCs are initially generated through coordination with a sacrificial metal such as Cu(ɪ) or Ag(ɪ), forming stable NHC–Cu(ɪ) and NHC–Ag(ɪ) complexes. These intermediates can subsequently undergo transmetalation with metal NPs to yield robust polymer–NHC–metal linkages. NHC-functionalized polymers can be prepared via postfunctionalization of polymers synthesized by atom transfer radical polymerization (ATRP). Typically, the terminal halogen group of the ATRP-derived polymer was first converted into an imidazolium or benzimidazolium moiety through alkylation with methylimidazole or methylbenzimidazole. Treatment of the resulting imidazole-terminated polymers with a mild bicarbonate base led to the formation of polymer–NHC–Cu(ɪ) or

Fig. 3 Two distinct methods for grafting NHC-functionalized polymer ligands onto metal NPs. (a) and (b) Scheme and photos showing the surface modification of AuNPs using PS–NHC–Cu(ɪ) (a) and (b) NHC–PS·HCO$_3^-$. Reproduced with permission.[126] Copyright 2020 The Royal Society of Chemistry.

This journal is © The Royal Society of Chemistry 2026

J. Mater. Chem. A, 2026, 14, 11848–11879 | 11855

polymer–NHC–Ag(I) complexes upon reaction with Cu_2O or Ag_2O.[127,128] These NHC–metal polymer ligands could be transferred onto citrate-capped metal NPs *via* biphasic ligand exchange at the water/toluene interface (~5 min), producing robust, polymer NHC-stabilized NPs (Fig. 3a). The second approach involves direct *in situ* generation of NHCs without using a sacrificial metal.[126] In this method, imidazolium- or benzimidazolium-containing polymers undergo counterion exchange with bicarbonate, which deprotonates imidazolium to produce "free" NHCs while releasing CO_2 and water. The freshly generated NHCs, owing to their high reactivity, can immediately coordinate to metal NP surfaces, even in poor solvents for the polymers, within approximately 1 min (Fig. 3b). Using these complementary ligand-exchange strategies, we have successfully prepared both monodentate and polydentate NHC-functionalized polymers with diverse backbones, including polystyrene, poly(meth)acrylate, and poly(meth)acrylamide, demonstrating broad applicability and versatility of the NHC-based surface modification approach.

Hydrophobic polymer-containing NHC ligands exert a pronounced influence on the selectivity of the eCO_2RR. We prepared three types of monodentate NHC-functionalized polymer ligands: hydrophilic poly(ethylene oxide) (NHC–$PEO·HCO_3^-$, P1), hydrophobic NHC–$PS·HCO_3^-$ (P2), and
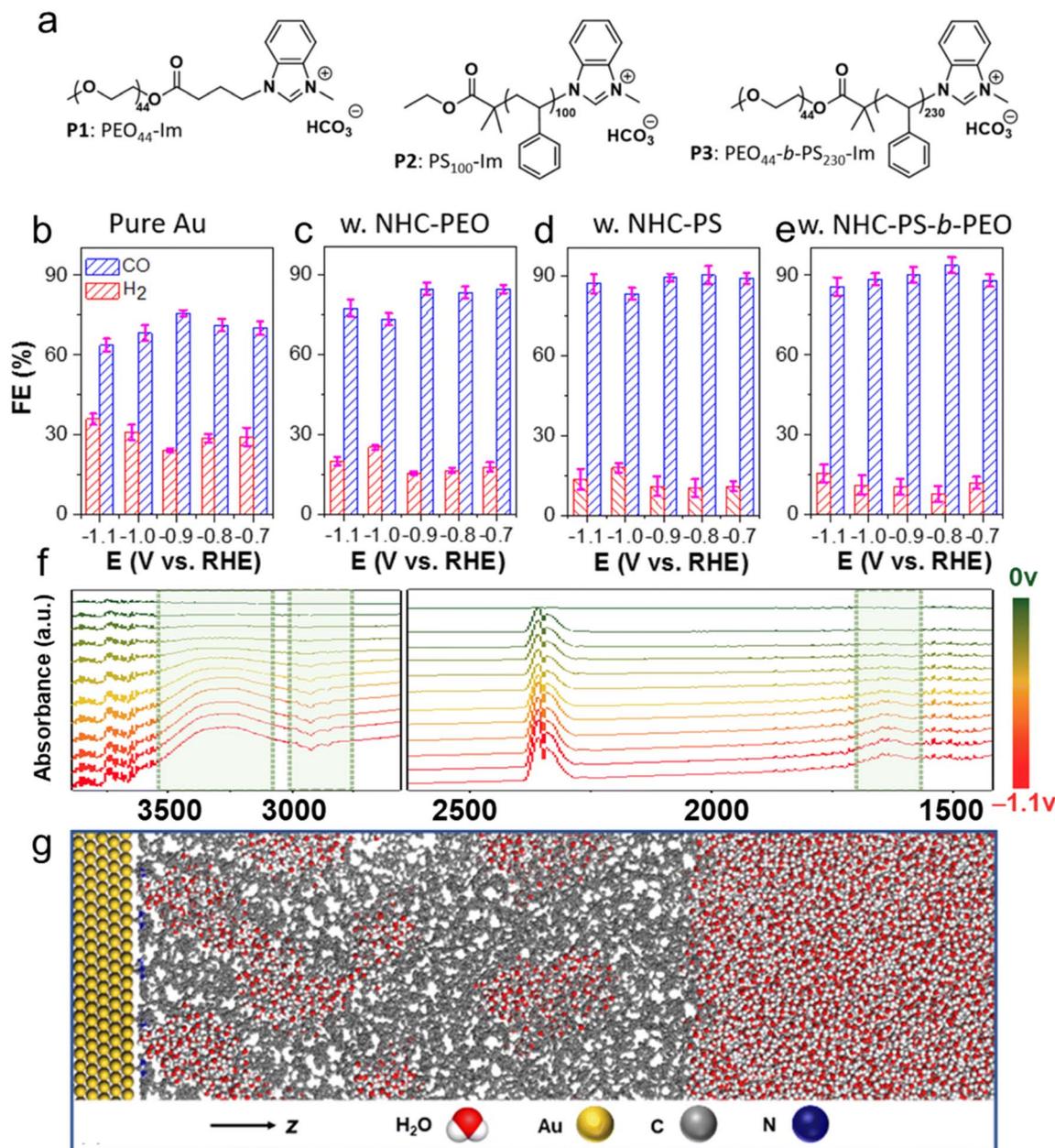
Fig. 4   (a) Chemical structures of NHC–$PEO·HCO_3^-$, (P1), NHC–$PS·HCO_3^-$ (P2), and NHC–PEO-*b*-$PS·HCO_3^-$ (P3). (b)–(e) CO and H_2 FE of Au (b), Au–P1 (c), Au–P2 (d) and Au–P3 (e). (f) *In situ* ATR-SEIRAS spectra of Au–P3, obtained at −0.3 V. (g) Molecular dynamics (MD) simulations showing the formation of water clusters at the catalyst–electrolyte interface. Reproduced with permission.[111] Copyright 2023 The Royal Society of Chemistry.

11856 | *J. Mater. Chem. A*, 2026, **14**, 11848–11879

This journal is © The Royal Society of Chemistry 2026

amphiphilic block copolymer NHC–PEO-b-PS·HCO_3^- (P3) (Fig. 4a).[111] These three polymer ligands were used to modify AuNPs supported on carbon, ensuring good electron conductivity between the electrode and the catalysts. The eCO_2RR performance was evaluated in 0.1 M $KHCO_3$ using an H-cell apparatus. Their performance was compared based on CO FE and their partial current density for CO (J_{CO}) and H_2 (J_{H_2}). As a control, the CO FE of Au/C varied in the range of 64% to 76% in the potential window of −0.7 to −1.1 V. The CO FE of Au–P2 and Au–P3 increased to about 90% in the same potential window, while the CO FE of Au–P1 was 80–85%, indicating that hydrophobic PS enhanced CO_2-to-CO selectivity (Fig. 4b–e). The J_{CO}/J_{H_2} ratio and the CO/H_2 product ratio for Au–P2 and Au–P3 were 8.1 and 8.5, respectively, roughly 3 times higher than that of unmodified Au/C.

Comparable enhancements were demonstrated upon modification of gold nanowires (AuNWs) with hydrophobic NHC–PS·HCO_3^- for the eCO_2RR. After modification, the CO FE reached >90% over an extended potential window (−0.4 to −1.0 V), whereas for unmodified Au NWs the CO FE reached >90% only from −0.5 to −0.7 V. The in $situ$ ATR-SEIRA showed that ~41% of water formed clusters with PS–NHC modified Au NWs due to strong hydrogen bonding, as compared with ~10% for unmodified AuNWs, suggesting that water was more confined for modified Au NWs. Meanwhile, the modified Au NWs showed robust stability because of the strong bonding between NHC groups with Au NWs; their CO FE retained >90% during 10 h of electrolysis, while that of unmodified Au NWs dropped rapidly to 58% after a 10 h test. In addition, the C_2H_4 FE reached 58% at −1.1 V by combining PS–NHC modified Au NWs with Cu NWs.[130]

To probe the interfacial mass transport behavior, three different molecular probes were used to examine the mass transfer process at the catalyst–electrolyte interface. The diffusion coefficient (D_0) of anionic probe $K_3Fe(CN)_6$ and cationic probe $Ru(NH_3)_6^{3+}$ slightly decreased for Au–P1, Au–P2 and Au–P3, in comparison with Au/C. However, for Au–P1 and Au–P3, the D_0 of hydrated probe ferrocenecarboxylic acid (Fc–COOH) is two times higher than that of Au/C (Fig. 4d). These results suggest that polymer ligands had a minimum effect on the mass transport of small ions, including protons. Additionally, the diffusion coefficient of CO_2 for Au–P2 and Au–P3 was ~3 times higher than that of Au/C, due to the hydrophobic PS domains that provided high solubility for CO_2. Attenuated total reflectance surface-enhanced infrared absorption spectroscopy (ATR-SEIRAS) confirmed that the polymer ligands did not inhibit water adsorption on the Au surface under negative bias. Notably, in the presence of hydrophobic polystyrene, the O–H stretching vibration of adsorbed water shifted to approximately 3300 cm^{-1}, from 3400 cm^{-1} for the Au control without polymers, signifying enhanced hydrogen bonding interactions (Fig. 4f). These spectral features indicate that, in the presence of hydrophobic PS ligands, water molecules became spatially confined at the catalyst–electrolyte interface, forming densely packed clusters with strengthened hydrogen-bond networks. Molecular dynamics (MD) simulations supported these findings, revealing a 5-fold increase in hydrogen-bond density near the hydrophobic PS domains (Fig. 4g). Consequently, the reduced solubility of CO_2 within these water clusters promoted its preferential dissolution and enrichment in the hydrophobic polymer regions, thereby facilitating CO_2 activation and reduction at the interface.

Compared with monodentate NHC-functional polymer ligands, polydentate NHC-functionalized polymers showed higher stability due to the multiple binding motifs. Polydentate NHCs were synthesized through the quaternization of poly(-vinylbenzyl chloride) with methyl benzimidazole (Fig. 5a).[85] After exchanging counterion with bicarbonate, the multi-NHC
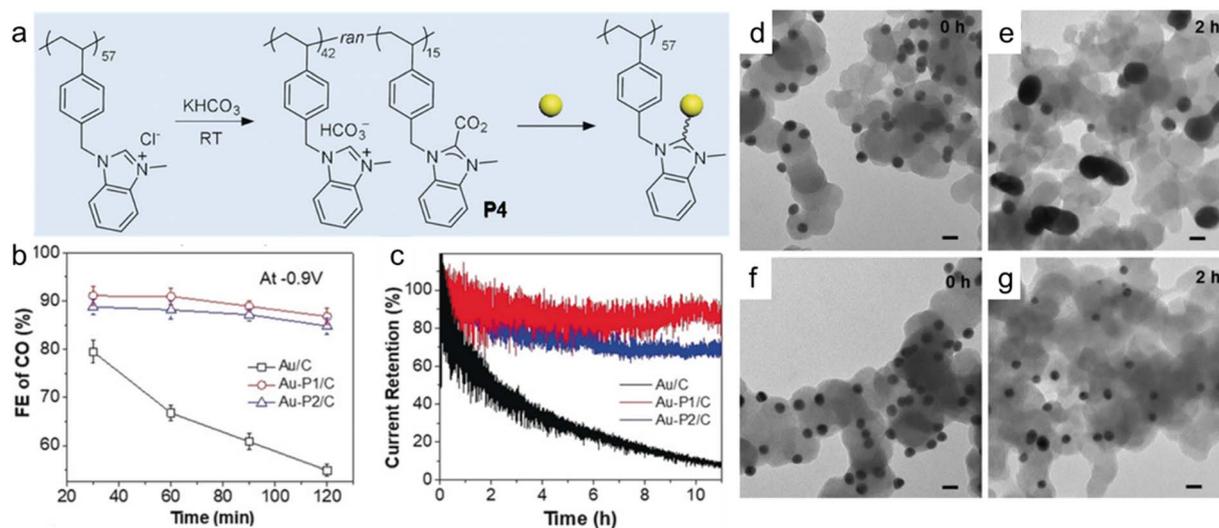

Fig. 5 (a) Synthesis of a polydentate NHC polymer with HCO_3^- as a counterion (P4) and surface modification of NPs (yellow). (b) CO FE at −0.9 V for different electrolysis times. (c) Long-term stability plotted as current retention $versus$ time at −0.9 V for 11 h. (d)–(g) TEM images of Au/C (d) and (e) and Au–P4/C (f) and (g) before (left) and after (right) CO_2 reduction at −0.9 V for 2 h. All scale bars are 20 nm. Reproduced with permission.[85] Copyright 2019 Wiley.

This journal is © The Royal Society of Chemistry 2026

J. Mater. Chem. A, 2026, 14, 11848–11879 | 11857

functionalized polymer (P4), consisting of poly(vinylbenzyl N-methylbenzimidazolium bicarbonate) (PVBMB-Im·HCO_3^-) and poly(vinylbenzyl N-methylbenzimidazolium carboxylate) (PVBMB-Im·CO_2) is air-stable and can be grafted to nano-catalysts under mild conditions (Fig. 5b). After electrolysis at −0.9 V for 2 h, the electrochemically active surface area (ECSA) of Au–P4/C slightly decreased by 22.3%. In comparison, unmodified Au/C showed a larger loss, ~75.3% of its initial ECSA. The initial CO FE values for Au–P4/C and Au/C were ~90% and 79%, respectively, while that of Au–P4/C decreased by ~4%. However, the CO FE of Au/C decreased by ~24% after 2 h of electroreduction, suggesting that Au–P4/C retained stable CO selectivity (Fig. 5c). The long-term stability was tested by chronoamperometry (i–t) at −0.9 V for 11 h. Au–P4/C showed only 14% current loss while unmodified Au/C exhibited ~90% current loss, suggesting the remarkable stability of Au–P4. The structural stability of Au–P4/C was confirmed by TEM. For Au/C, large aggregates formed after 2 h of reduction, while the AuNPs were much more stable than P1 modified AuNPs (Fig. 5d–g).

Other than AuNPs, polydentate NHCs also were examined for commercial Pd/C. The commercial Pd/C catalyst had ultrasmall Pd of about 3–5 nm and was not selective for the eCO₂RR with about 40% FE of CO. The selectivity of Pd–P4/C increased to 62% of CO and 3.5% of formate. The catalyst's stability improved remarkably after P4 modification. The ECSA loss of commercial Pd/C was 91.3%, while that of Pd–P4/C decreased by only 28.9% at −1.26 V for 2 h of electrolysis. Hence, NHC-functionalized polymer ligands not only enhance NP stability but also leverage polymer hydrophobicity to facilitate CO_2 transport to the catalyst surface.

Local hydrophobicity in the eCO₂RR is important, but it does not require chemical grafting of polymers onto NPs. Polymer binders, for example, are often used to anchor catalysts onto electrode surfaces, ensuring mechanical stability and efficient ion transport within electrochemical systems.[131] In many cases, their properties influence the local reaction environment, particularly the wettability of catalysts against the electrolyte. Pham *et al.* studied different polymer binders: hydrophilic polyacrylic acid (PAA) and hydrophobic fluorinated ethylene propylene (FEP) and Nafion to mix with CuO and prepared the electrode.[132] The HER was suppressed with FEP and CuO–Nafion. The highest (C_{2+}) FE of 52% was observed on CuO–FEP at −1.1 V at a partial current density of 37.4 mA cm^{-2}, while the (C_{2+}) FE values of CuO–Nafion and CuO–PAA were ~43% and 35%, respectively. For hydrophilic Cu–PAA, the catalyst surface is fully wettable by the electrolyte and the localized proton concentration is significantly higher, resulting in a substantially higher H_2 FE (~38% at −1.1 V). The hydrophobicity of these polymer binders was evaluated by using the WCA and the captive bubble contact angle measurements. The WCAs of CuO–FEP, CuO–Nafion, and CuO–PAA were 144°, 132° and 32°, respectively, while their captive bubble contact angles were 47°, 73° and 117°, respectively. By strategically manipulating surface wettability, one can modulate the local microenvironment, namely wettability of catalysts and transport rates of water, which are important for the competition between desired CO_2-reduction and unwanted HER pathways.

4. Conductive polymer ligands for the eCO₂RR

Although typical hydrophobicity of polymers (*e.g.*, PTFE) can enhance eCO₂RR performance by increasing the local CO_2 concentration and suppressing the HER, it also increases transfer resistance (*i.e.*, the electrode to catalysts), leading to high cathode overpotential and low energy efficiency in the eCO₂RR. To balance hydrophobicity and conductivity, one can physically mix nanocatalysts with conductive materials. For example, a superhydrophobic, highly conductive and hierarchical wire membrane consisting of core–shell CuO NPs, carbon nanotubes and PTFE was prepared by thermal annealing of electrospun fibers containing PEO, Cu_2O NPs and PTFE NPs, labelled as CuO/F/C(w).[133] The eCO₂RR of CuO/F/C(w) was performed in a H-cell with CO_2 saturated 0.5 M KHCO₃ solution. Compared with 10.1% FE(C2–3) of bare CuO and 37.6% FE(C2–3) of the mixture of carbon nanotubes, Cu_2O NPs and PTFE NPs (CuO/F/C(m)), the maximum FE(C2–3) of CuO/F/C(w) is 56.8% at −1.4 V because of its excellent hydrophobicity/conductivity and highly exposed CuO NPs.

Conductive polymers are conjugated polymers with high electronic conductivity that modulate both conductivity (electrons and ions) and hydrophobicity.[78] A continuous electrodeposition can be used to coat various conductive polymers, *e.g.*, polyaniline (PANI), polypyrrole (PPy), polythiophene (PTh), and their copolymers, together with metal catalysts (*e.g.*, Cu, Pd, Zn, and Sn) on carbon paper (CP), serving as an electrode for the eCO₂RR (Table 1).[134] Taking Cu/PANI–CP (I) as an example, the 3D network of PANI nanofibers acts as a matrix for electrodeposition of Cu nanosheets. Compared to conventional methods, including drop-coating of CuNPs on PANI (Cu/PANI–CP (II)), drop-coating solvothermal synthesis of CuNPs on PANI (Cu/PANI–CP (III)) and direct electrodeposition of CuNPs on CP (Cu–CP (IV)) (Fig. 6a), Cu nanosheets were well-dispersed in the PANI network that endowed it with high ECSA, excellent eCO₂RR performance and improved long-term stability, as confirmed by the electrolysis of CO_2, which was carried out in CO_2-saturated 0.1 M KCl using a H-cell. Cu/PANI–CP (I) had much higher C_2H_4 FE (~58% at −1.2 V) than other catalysts (Fig. 6b). EIS indicated that the interfacial charge transfer resistance of Cu/PANI and PANI/CP was reduced or eliminated due to the well-contacted structure in Cu/PANI–CP (I). The film resistance between the catalyst and substrate and charge transfer resistance between the electrolyte and Cu/PANI–CP (I) was much smaller than these in other control catalysts (Fig. 6c). As shown in Fig. 6d, Cu/PANI–CP (I) balanced the fast electron transfer and CO_2 diffusion as a result of its well-dispersed Cu nanosheets and enhanced conductive network.

Similarly, Huang *et al.* fabricated Cu/PANI–CP by sequentially spray-coating CuNPs and PANI on CP. The conductivity and hydrophobicity of PANI can be tuned *via* using various acids to modify PANI (Fig. 6e and f), *e.g.* H_2SO_4, *p*-aminobenzenesulfonic acid (ABSA) and dodecylbenzene-sulphonic acid (DBSA), labelled as H_2SO_4–PANI, ABSA–PANI, and DBSA–PANI.[135] The distribution of relaxation time analysis

11858 | *J. Mater. Chem. A*, 2026, **14**, 11848–11879
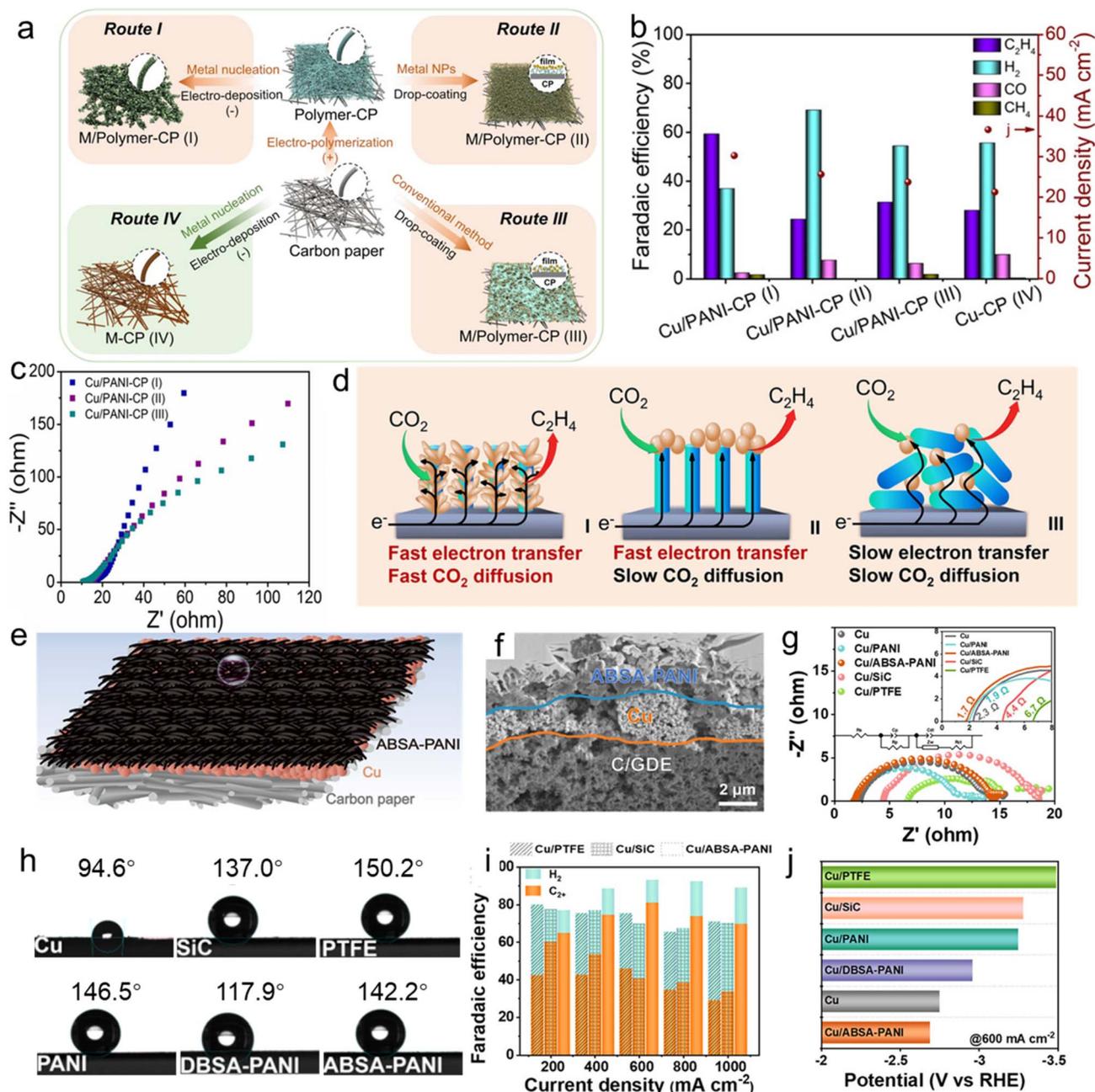
This journal is © The Royal Society of Chemistry 2026

Fig. 6 (a) Process used to prepare various electrodes. (b) Product distribution and average current density over different electrodes. (c) Nyquist plots of Cu/PANI–CP (I), Cu/PANI–CP (II), and Cu/PANI–CP (III) electrodes in CO_2-saturated 0.1 M KCl solution at equilibrium potential for the eCO_2RR. (d) CO_2 diffusion and electron transfer on various Cu/PANI–CP electrodes with different structures. Reproduced with permission.[134] Copyright 2021 Wiley. The scheme (e) and cross-sectional SEM image (f) of the ABSA–PANI/Cu/C electrode. Water contact angle (g) and Nyquist plots (h) of Cu, SiC, PTFE, PANI, DBSA–PANI, and ABSA–PANI. (i) Comparison of product distribution for Cu/PTFE, Cu/SiC, and Cu/ABSA–PANI in flow cells with 0.05 M H_2SO_4 and 1 M KCl. (j) Comparison of voltages consumed by different electrodes to achieve 600 mA cm^{-2}. Reproduced with permission.[135] Copyright 2025 Wiley.

on EIS data showed the lowest peak intensity for Cu/ABSA–PANI in the low frequency region, demonstrating that Cu/ABSA–PANI has excellent electron and ionic conductivity. Additionally, Cu/ABSA–PANI–CP showed a lower internal resistance (1.7 Ω) than common hydrophobic molecules (PTFE, 6.7 Ω and SiC, 4.4 Ω), significantly decreasing ohmic polarization and potential loss (Fig. 6g). Acid-doped PANI chains also exhibited much lower

interfacial electron transfer resistance than PANI. In comparison with H_2SO_4–PANI and DBSA–PANI, the strong steric hindrance effect of ABSA resulted in PANI chains becoming more extended, leading to higher conductivity and lower charge transfer resistance. Meanwhile, the hydrophobicity of PANI was well-retained for ABSA–PANI with a WCA of 142° (Fig. 6h). The eCO_2RR was performed in a mixture of 1 M KCl and 0.05 M

This journal is © The Royal Society of Chemistry 2026

J. Mater. Chem. A, 2026, **14**, 11848–11879 | **11859**

H_2SO_4 (pH = 1). The maximum (C_{2+}) FE of Cu/ABSA–PANI–CP reached 81% at 600 mA cm^{-2}, higher than that of Cu–CP ($\sim$34%) and Cu/ABSA–PANI–CP ($\sim$70%) (Fig. 6i). Meanwhile, Cu/ABSA–PANI–CP was stable over 11 h at 600 mA cm^{-2} with (C_{2+}) FE >60%. After modification using acids, Cu/ABSA–PANI–CP adsorbed 2.1 times more K$^+$ than Cu–CP because of the electrostatic interaction between –SO$_3^-$ and K$^+$, resulting in high performance at low concentrations of alkali cations. The CO$_2$/Ar partial pressure experiment and DRT analysis on the EIS data indicated that Cu/ABSA–PANI–CP was insensitive to the variation of CO$_2$ concentration, suggesting that the ABSA–PANI polymer layer is conducive to CO$_2$ adsorption and retains a high local CO$_2$/H$_2$O concentration ratio, thereby facilitating the eCO$_2$RR. Compared with hydrophobic polymers (PTFE, −3.5 V) or hydrophobic coating (SiC, −3.3 V), it required only −2.6 V for Cu/ABSA–PANI to reach a current density of 600 mA cm^{-2} (Fig. 6j), suggesting that conductive PANI improves the energy efficiency.

Poly(3,4-ethylenedioxythiophene) (PEDOT) is another widely used conductive polymer and it is commonly employed as a flexible electrode material in organic electronics.[136–138] Meanwhile, the thiophene (Th) of EDOT units can coordinate with other metal ions, enabling the construction of metal–polymer hybrid catalysts. Han et al. prepared a novel layered coordination polymer (Cu–PEDOT) through in situ redox polymerization of EDOT and copper chloride. As a weak oxidant, Cu^{2+} drove the polymerization of EDOT while Cu^{2+} was trapped in PEDOT particles with a Cu to S ratio of 1 : 1.2. The hybrid catalysts had a high conductivity of 6 × 10^{-2} S m^{-1}.[139] In a three-compartment flow cell with 1 M KOH, Cu–PEDOT showed a CH$_4$ FE of 62.7% at −1.58 V, about 1.6, 2.1, and 2.4 times higher than that of CuO (39.1%), CuS (0.3%), and Cu (26.3%). DFT calculations suggested that the d-band center of Cu–PEDOT had a 0.4 eV positive shift, as compared to that of pure Cu, leading to favorable adsorption of *CO. The strong binding of *CO promoted deep reduction to CH$_4$ along with the exothermic steps of *CO$_2$ to *COOH (−1.04 eV) and *CO to *CHO (−0.51 eV).

In addition, the selectivity of the eCO$_2$RR can be varied by proton shuttling mechanisms in conductive polymers. With PANI and PPy impregnated Cu-based MOF (HKUST-1), CH$_4$ was the main product for PPy@HKUST-1 with a maximum FE of 55.5% at 250 mA cm^{-2}, while C$_2$H$_4$ is the main product for PANI@HKUST-1 with an FE of 67.5% at 600 mA cm^{-2}, in comparison to HKUST-1 with a CO FE for the maximum C$_2$H$_4$ reaching 67.5% at 600 mA cm^{-2} at 100 mA cm^{-2} (Fig. 7a).[140] In attenuated total reflection surface enhanced infrared spectroscopy (ATR-SEIRAS), for PPy@HKUST-1, the intensity of H–OH bending (1591 cm^{-1}) and H–C=O stretching (1235 cm^{-1}) of *CHO synchronously enhanced with the increase of reduction
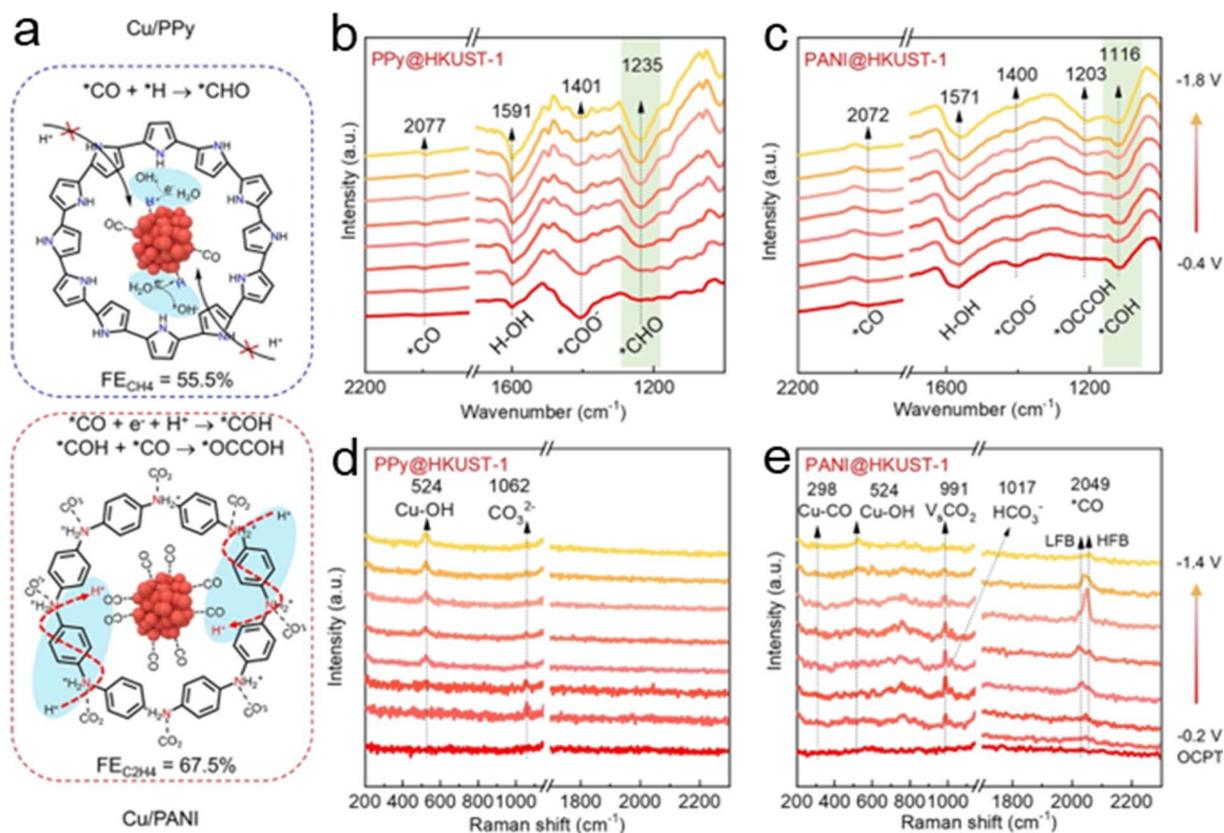

Fig. 7 (a) Proposed mechanism for the MOF-derived Cu/PPy and Cu/PANI interfaces to steer the eCO$_2$RR pathway. ATR-SEIRAS spectra of (b) PPy@HKUST-1 and (c) PANI@HKUST-1. Raman spectra of (d) PPy@HKUST-1 and (e) PANI@HKUST-1 during the eCO$_2$RR. Reproduced with permission.[140] Copyright 2023 Wiley.

11860 | J. Mater. Chem. A, 2026, 14, 11848–11879

This journal is © The Royal Society of Chemistry 2026

potential, indicating that (i) *CHO was formed by coupling *CO and *H and (ii) *CHO mediated the formation of CH$_4$. For PANI@HKUST-1, apart from the common intermediates of *CO (2072 cm^{-1}) and *COO$^-$ (1400 cm^{-1}) observed for PPy@HKUST-1, a strong peak of C=O stretching is observed at 1116 cm^{-1} (Fig. 7b and c), attributed to *COH. In addition, the peak intensity at 1203 cm^{-1}, corresponding to *OCCOH, increased with potential. The intensity of H–OH bending showed no significant increase with potential, suggesting that the high *CO coverage led to the asymmetric coupling of *COH and *CO. Further *operando* Raman spectroscopy also confirmed high *CO coverage for PANI@HKUST-1, evidenced by peaks at 298 cm^{-1} (Cu–CO rotation) and 2033–2049 cm^{-1} (C≡O stretching) (Fig. 7d and e). In comparison, PPy@HKUST-1 exhibited Cu–OH species at 524 cm^{-1}. DFT calculations suggested that PPy@HKUST-1 showed a much lower activation barrier for surface *H formation (0.57 eV) than PANI/Cu (1.63 eV), enabling easier protonation of adsorbed *CO to *CHO, which favors CH$_4$ formation at moderate to low *CO coverage. The proton shuttling *via* benzenoid –NH– on PANI/Cu has a favorable barrier (0.53 eV) and small free energy change (0.15 eV) for reducing *CO to *COH, using protonated –NH$_2^+$– as the hydrogen source, whereas O-protonation of *CO is less favorable (2.1 eV), aligning with observed *COH formation and subsequent coupling to OCCOH and further hydrogenation to C$_2$H$_4$.

5. Ionic polymer ligands for the eCO$_2$RR

Ionic polymers, which balance ionic functionality and hydrophobicity to modulate interfacial ionic conductivity and water accessibility, have also attracted much attention for the eCO$_2$RR. By precisely tuning the content and distribution of ionic groups within the polymers, one can control the interfacial properties. A higher density of ionic groups enhances proton or water transport through ion–dipole interaction, whereas incorporating hydrophobic segments can facilitate CO$_2$
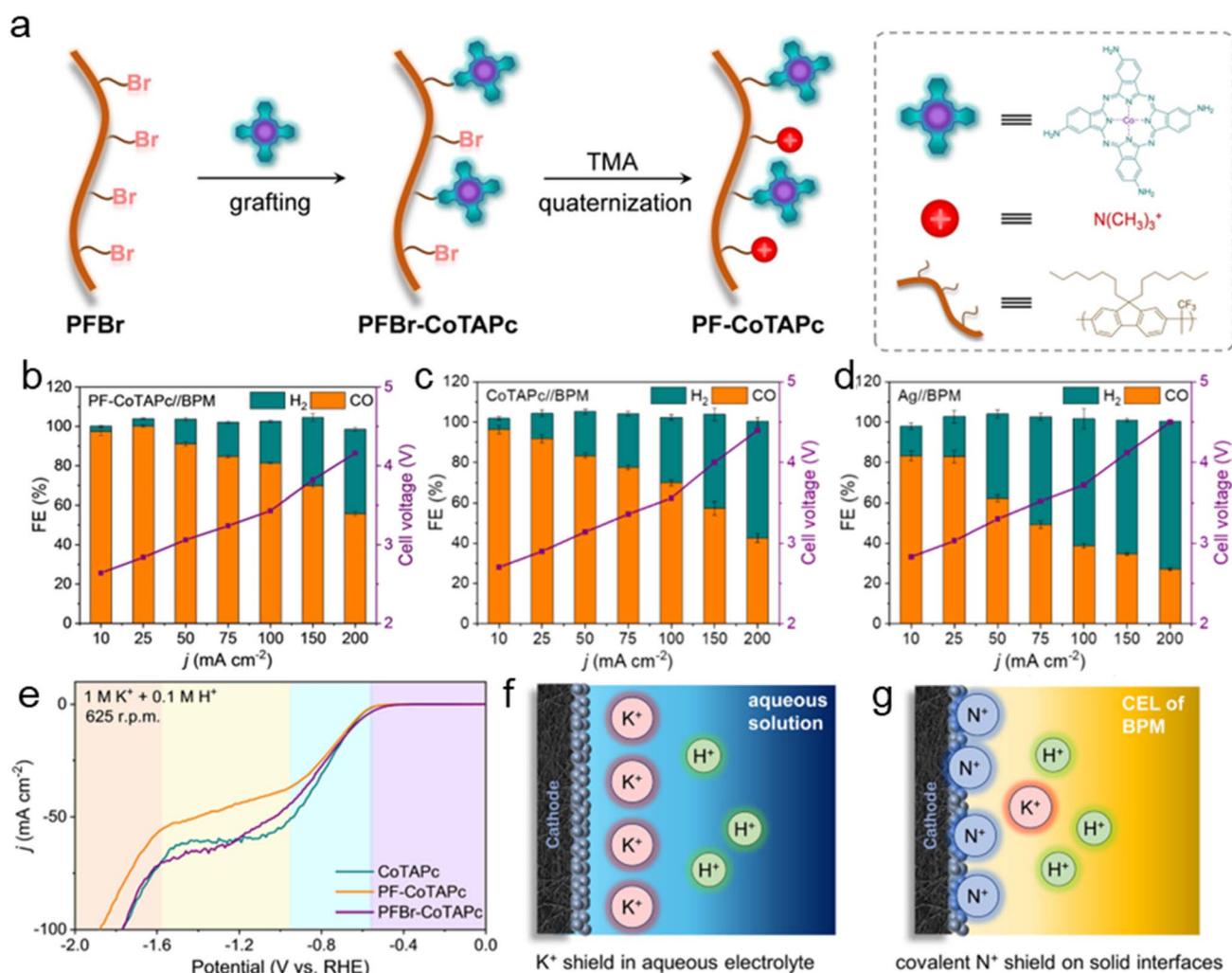

Fig. 8 (a) Synthesis of polymeric catalyst PF–CoTAPc. (b)–(d) CO, H$_2$ FE and cell voltage of PF–CoTAPc (b), CoTAPc (c) and Ag (d) in a BPM-based zero-gap electrolyzer. (e) LSV curves collected at a scan rate of 40 mV s^{-1} in N$_2$-saturated solutions (1 M K$^+$ and 0.1 M H$^+$) at rotating speeds of 625 rpm. (f) and (g) Illustration of local fields at the diffusion layers for (f) conventional method with high-concentration alkali metals and (g) covalent grafting of quaternary ammonium groups. Reproduced with permission.[141] Copyright 2024 Wiley.

This journal is © The Royal Society of Chemistry 2026

J. Mater. Chem. A, 2026, 14, 11848–11879 | 11861

diffusion. Ye *et al.* designed positively charged polyfluorene (PF) by covalently grafting cobalt tetraaminophthalocyanine (CoTAPc) through the successive reaction between CoTAPc/ trimethylamine (TMA) and bromoalkyl polyfluorene (PFBr) (Fig. 8a).[141] The positively charged backbones in the microenvironment near the active sites were thought to lower the proton concentration. In a H-cell test, the CO FE and J_{CO} of PF–CoTAPc reached 98.6% and -22.5 mA cm^{-2} at -0.8 V, while the CO FE and J_{CO} of CoTAPc were 90.8% and -13.7 mA cm^{-2}. The CO production rate (TOF$_{(ICP)}$) of PF–CoTAPc was 2.0 s^{-1} at -0.8 V, higher than that of CoTAPc (1.2 s^{-1}). Given the well-dispersed active Co sites within ionic polymers, the surface accessible Co sites of PF–CoTAPc were about 1.6 times those of CoTAPc. In a bipolar membrane (BPM) electrolyzer, PF–CoTAPc also showed a CO FE of 82.6% at 100 mA cm^{-2}, as compared to that of CoTAPc, $\sim$69.3% (Fig. 8b–d). Rotating disk electrode (RDE) voltammetry, performed in the N$_2$-saturated 0.05 M H$_2$SO$_4$ with 3 M KCl electrolyte, showed typical diffusion limiting current in the range of -0.9 to -1.6 V (Fig. 8e). A much smaller HER current for PF–CoTAPC was seen, as compared to that of CoTAPc and PFBr–CoTAPC. Hydrophobic PF–CoTAPc obviously limited proton diffusion. To minimize the impact of K$^+$ known to enhance eCO$_2$RR performance due to the ion repulsion between K$^+$ hydrates and protons (Fig. 8f), the eCO$_2$RR was further carried out in 0.05 M H$_2$SO$_4$ with 0.01 M KCl. PF–CoTAPC still reached the highest CO FE at a lower overpotential in comparison with the other two catalysts. These results suggested that the HER was suppressed by the quaternary ammonium groups to improve the overall selectivity of the eCO$_2$RR under acidic conditions (Fig. 8g).

The incorporation of ionic polymers as binders has proven equally critical for optimizing the performance of metal NPs. As aforementioned, ionic polymers actively modulate the interfacial microenvironment surrounding the catalytic surface. Ionic polymers contain different charged groups, such as sulfonate, quaternary ammonium, or imidazolium moieties that create ion-selective domains at the electrode–electrolyte interface. These charged regions govern the transport of reactive species, including protons, hydroxide ions, and bicarbonates, and can drastically influence the competition between CO$_2$ reduction and the HER. For example, polycations, including commercially available Sustainion, containing quaternary ammonium or imidazolium groups, favor the accumulation of bicarbonate and hydroxide anions near catalysts. For example, Bell and co-workers used Sustainion (ammonium) and Nafion (sulfonate) to construct ionic bilayers on the Cu surface to regulate pH, local water and CO$_2$ concentration. The coating of both ionomers resulted in 80% (C$_{2+}$) FE at -1.15 V.[142] The anionic Nafion enhanced CO$_2$ transfer, while the cationic layer increased the local pH and both layers changed the water concentration. In a related study, Ngene *et al.* used Cu$_2$O nanocubes as model catalysts and mixed them with Sustainion or Nafion as a binder and compared their catalytic behaviors.[143] Five electrodes were prepared by mixing Cu$_2$O nanocubes with Nafion or Sustainion, including no binder (as control), Nafion, Sustainion, Naf–Sus and Sus–Naf (note: Naf–Sus indicates two layers: the first layer is Cu$_2$O nanocubes with Nafion and the last layer is pure

Sustainion and *vice versa*). The eCO$_2$RR results showed that all electrodes containing Nafion had a low H$_2$ FE and high FE towards C$_{2+}$ due to suppressing the HER and promoting eCO$_2$RR activity. The presence of the cationic polymer binder enhanced the ratio of ethanol to ethylene. For Cu$_2$O nanocubes without a binder, the reduction of protons or H$_2$O resulted in the accumulation of OH$^-$. It served as a proton acceptor from bicarbonate which buffers the local pH by reacting with OH$^-$ to form CO$_3^{2-}$, while K$^+$ balanced negatively charged species that improve the water-mediated HER and eCO$_2$RR. On the other hand, the positively charged Sustainion favored bicarbonate anions and repelled K$^+$, resulting in bicarbonate precipitation in the Sustainion layer. Hence, the ECSA, current density and C$_{2+}$ selectivity showed a large decrease of 43%, 66% and 50% after 20 h of electrolysis. However, the negatively charged sulfonate of Nafion blocked OH$^-$ and CO$_3^{2-}$ transport and increased the abundance of K$^+$, thereby suppressing the HER. Similarly, the effect of charged polymer binders among Nafion, Sustainion and the anion-exchange polymer binder with m-ethylimidazolium groups (PiperION) on the eCO$_2$RR was compared using AgNPs as catalysts.[144] Compared to binder-free AgNPs, the H$_2$ FE and HCOO$^-$ FE of Nafion coated AgNPs increased by 3$\sim$4%, while HCOO$^-$ FE of Sustainion coated AgNPs increased by 6.6%. Among the three binders, the H$_2$ FE of PiperION coated AgNPs increased by 15.9% due to hydrophilicity. Sustainion coated AgNPs had the lowest ECSA yet they exhibited the best eCO$_2$RR with a CO FE of >99% because of the improved CO$_2$ availability.

Perfluorinated sulfonic acid (PFSA) is a typical hydrophobic/ ionic polymer, which efficiently improves CO$_2$ and ion mass transfer. Sargent's group demonstrated that PFSA ionomer coated Cu catalysts were highly selective for CO$_2$ reduction (>90% with 65–75% to C$_2$H$_4$).[145] The hydrophobic (CF$_2$)$_n$ domains on the Cu surface provided continuous percolating hydrophobic pathways for the diffusion of non-polar gas reactants while limiting the access of protons/water. This drawback is not critical in flow-cell reactors, where the catalyst layer is thin and gas diffusion occurs efficiently over micrometer-scale distances. In contrast, in traditional H-type reactors with limited mass transport, excessive hydrophobic coating can severely restrict both electron transfer and ion access to the catalyst surface, significantly slowing down the electroreduction process.[116] Furthermore, PFSA has a good selectivity for CO$_2$ mass transport from PFSA to the nanocatalyst surface.[146] In particular, the local CO$_2$ and H$_2$O mass transfer can be tuned by varying the side-chain lengths of PFSA. For example, Wang *et al.* achieved precise regulation of CO$_2$/H$_2$O ratios by incorporating CuNPs with PFSA ionomers containing tunable side-chain lengths.[147] DFT calculations suggested that PFSA with a long side-chain (LSC-PFSA) has higher binding energy with H$_2$O and lower binding energy with CO$_2$, suggesting a stronger CO$_2$ affinity, compared with PFSA with a short side-chain (SSC-PFSA). With the increase of side-chain lengths, the hydrophobicity of PFSA ionomers increases. Meanwhile, the hydrophobicity decreases as the ratio of the catalyst and ionomer (C/I ratio) decreases. The improved CO$_2$ capability and suppressed H$_2$O transport led to 89.4% FE(C$_{2+}$) at 536 mA cm^{-2} for LSC-
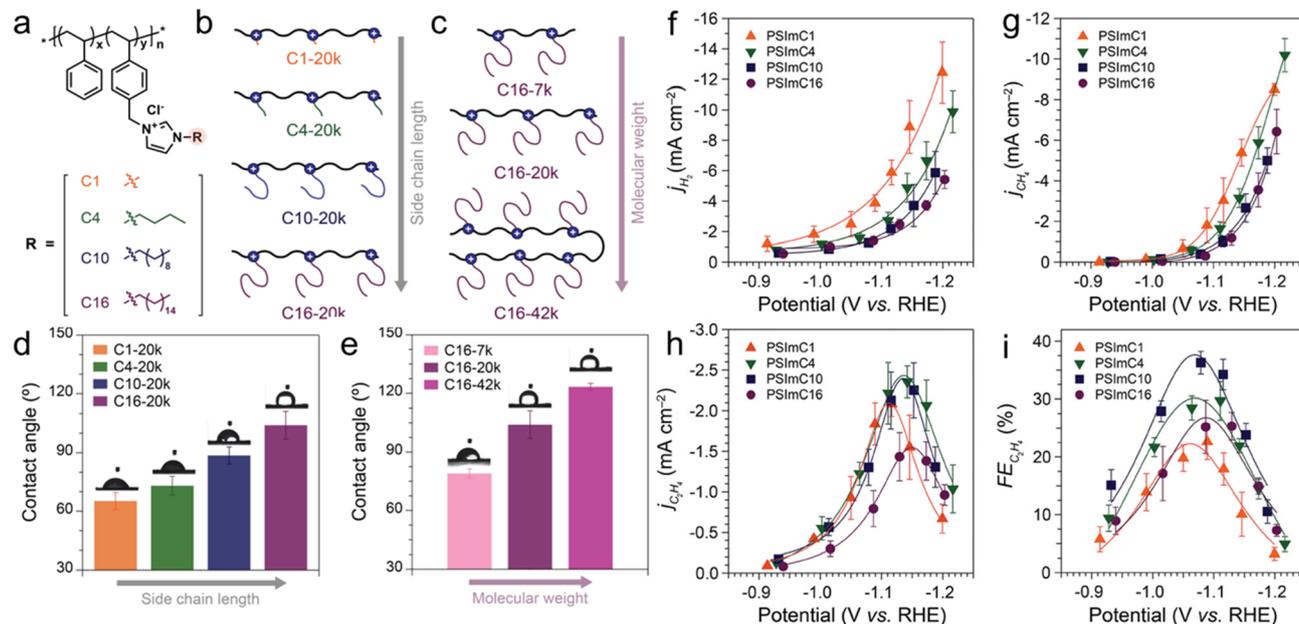
11862 | *J. Mater. Chem. A*, 2026, **14**, 11848–11879

This journal is © The Royal Society of Chemistry 2026

Fig. 9 (a) Chemical structures of 1-n-alkylimidazolium ionomers with n-alkyl side chains of varying lengths: methyl (C_1), n-butyl (C_4), n-decyl (C_{10}), and n-hexadecyl (C_{16}). (b) and (c) Schematic illustrations of ionomers with systematic variations in (b) side chain length (C_1-, C_4-, C_{10}-, and C_{16}-20k) at a fixed molecular weight of 20 kg mol^{-1} and (c) molecular weight (C_{16}-7k, C_{16}-20k, and C_{16}-42k) at a fixed alkyl side chain length of C_{16}. Contact angles of PSIm with (d) longer alkyl side chains and (e) higher molecular weights of the ionomers. Partial current densities for H_2 (f) CH_4 (g) and C_2H_4 (h) during the eCO$_2$RR at different applied potentials in CO_2-saturated 0.1 M KHCO$_3$. (i) C_2H_4 FE measured after electrolysis for 1 h. Reproduced with permission.[148] Copyright 2025 American Chemical Society.

PFSA. *In situ* ATR-SEIRAS indicated that LSC-PFSA showed an obvious *CO signal (~2060 cm^{-1}) at a lower potential and a relatively low H_2O signal (~3500 cm^{-1}), compared with SSC-PFSA, suggesting enhanced CO_2 transfer and suppressed H_2O.

On the other hand, positively charged polymers with similar structural features to Sustainion can serve as binders for metal nanocatalysts because of their ionic conductivity. The hydrophobic–hydrophilic balance determines how water and CO_2 molecules access the catalyst surface, directly impacting catalytic efficiency. The copolymer of poly(styrene-*co*-4-vinylbenzyl chloride) (PS-*co*-4VBC) can be converted to positively charged ammonium using alkylation, *e.g.*, 1-n-alkylimidazolium. The impacts of side chain lengths and molecular weight of positively charged polymer binders were systematically studied by Koh and colleagues (Fig. 9a–c).[148,149] WCAs increased from 65° for C_1-20k to 104° for C_{16}-20k and reached 123° for C_{16}-42k (Fig. 9d and e). Imidazolium functionalized PS-*co*-4VBC polymers with different n-alkyl side chains (PSImC$_n$ = 1, 4, 10, and 16) were synthesized and these polymer binders were mixed with commercial CuNPs and the eCO$_2$RR was conducted in a H-cell using CO_2-saturated 0.1 M KHCO$_3$ as electrolyte. The results showed that both the HER and CH_4 production were hindered as the side chain length increased. For example, the J_{H_2} of Cu–PSImC$_{16}$ decreased by 56.5% at -1.20 V and J_{CH_4} of Cu–PSImC$_{16}$ shifted from -3.0 to -1.2 mA cm^{-2} at -1.13 V, compared to those of Cu–PSImC$_1$ (Fig. 9f and g). However, the peak of $J_{C_2H_4}$ increases by 13.0% from Cu–PSImC$_1$ to Cu–PSImC$_4$ and Cu–PSImC$_{10}$ and then decreases by 36.2% from Cu–PSImC$_{10}$ to Cu–PSImC$_{16}$, indicating PSImC$_{10}$ with optimized chain length for C_2H_4 selectivity (Fig. 9h and i). DFT calculations suggested that

imidazolium moieties and the larger steric bulk of the long alkyl side chains hindered the interaction between the Cu (111) surface and protons, thereby decreasing the *H surface coverage and slowing HER kinetics. The *CO intermediate was more stable than the *HCO intermediate with the increase of chain lengths. Meanwhile, the activation energy of the proton coupled electron transfer (PCET) step was impeded, leading to the restricted overall kinetics of CH_4 formation. Contrastingly, the *2CO state was more stable with increasing alkyl chain length, facilitating the reaction kinetics of C–C coupling for C_2H_4 formation. A hydrophobic environment provided by PSImC$_n$ with long side chains led to a lower local water concentration and an increase of CO_2 and the *CO intermediate, hence suppressing the HER and CH_4 production. Moreover, polymer chain lengths also had a role in controlling the selectivity of CO_2 reduction. Using PSImC$_{16}$ modified AgNPs (molecular weights of polymer chains are 7–42 kg mol^{-1}), PSImC$_{16}$ with 20 kg mol^{-1} had the highest selectivity to C_2H_4 with an FE of 52.4%, due to suitable ion dissociation and polymer segmental mobility.

Quaternary ammonium groups are excellent binding motifs for metal NPs and they have been extensively used in the design of polyhedral NPs.[150–152] Our group designed polymer ligands with ammonium head groups and demonstrated that those polymers could modify various metal NPs.[153] The synthesis of such polymer ligands made use of alkylation of halogen-terminated polystyrene (PS) prepared *via* ATRP with N,N,N',N'-tetramethylethylenediamine, followed by further quaternization of their tertiary amines with iodomethane. These bidentate polymers (P5, Fig. 10a) with two ammonium head groups could
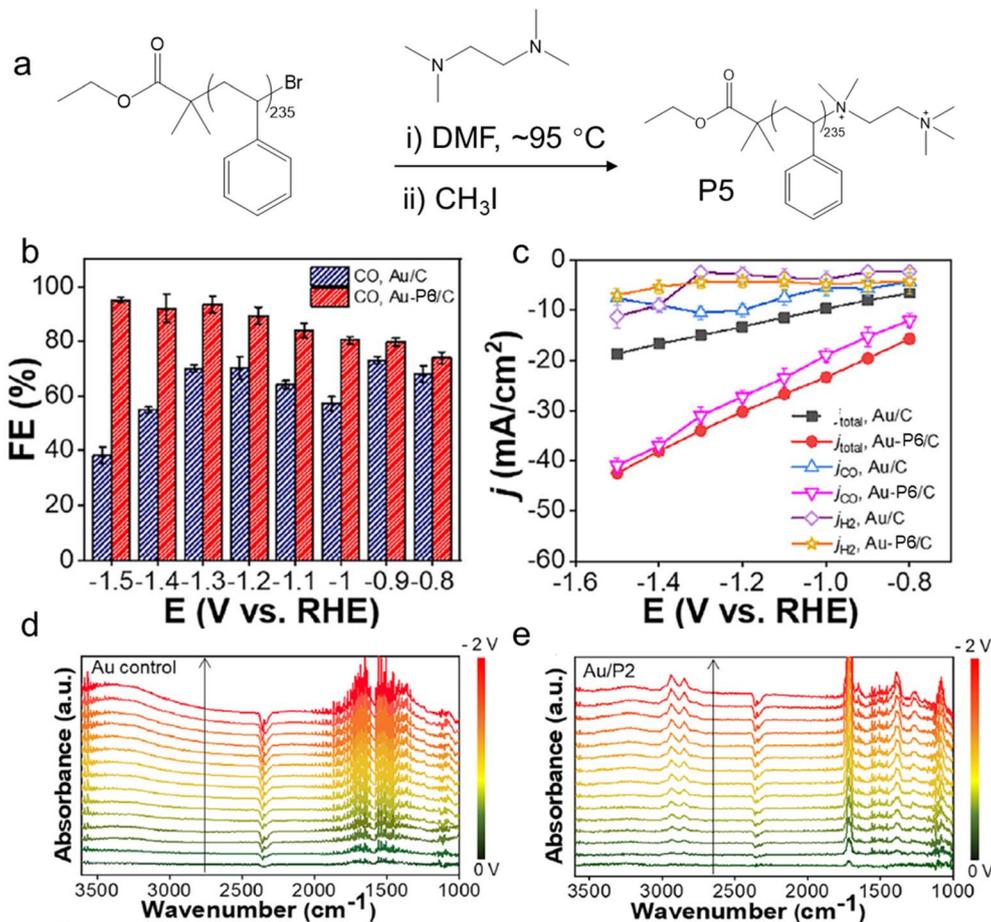
This journal is © The Royal Society of Chemistry 2026

J. Mater. Chem. A, 2026, 14, 11848–11879 | 11863

Fig. 10 (a) Synthesis of quaternary ammonium-containing polymers, P5. CO FE of Au/C (b) and Au−P5/C (c). *In situ* ATR-SEIRAS spectra of the Au control (d) and Au−P5 (e) within the range of 0 to −2 V with an interval of about −134 mV. Reproduced with permission.[153] Copyright 2025 Wiley.

modify citrate-capped metal NPs through biphasic phase transfer by mixing aqueous metal NPs with a toluene solution of P5. Such quaternary-ammonium containing hydrophobic polymers can introduce an ionic layer at the catalyst–electrolyte interface. In CO_2 electrolysis (H-cell, 0.1 M $KHCO_3$), unmodified Au/C exhibited a CO FE of 50–70% from −0.8 to −1.3 V, falling to 38% at −1.5 V due to mass-transport limitations by the low CO_2 solubility. In contrast, Au/C modified with P5 retained >94% CO FE even at −1.5 V, with a continuously increasing partial CO current density J_{CO} of ∼−41 mA cm^{-2} and nearly constant H_2 partial current J_{H_2} of −7 mA cm^{-2} (Fig. 10b and c). Quaternary ammonium-functionalized polymer ligands with a thin layer of ionic head groups can significantly improve both CO_2 reduction selectivity and catalyst durability through interfacial stabilization and local environment modulation.

ATR-SEIRAS was used to probe the change of the catalyst–electrolyte interface under CO_2 reduction conditions. With the Au control, spectra collected during a cathodic sweep from 0 to −2.0 V revealed a broad O–H stretching band near 3450 cm^{-1} from adsorbed water, whose intensity increased with negative bias, consistent with water dipoles aligning with H-down on the negatively charged electrode (Fig. 10d). In the presence of P5, this O–H band redshifted to 3230 cm^{-1}, about 220 cm^{-1} lower

than that on bare Au (Fig. 10e). This is consistent with hydrophobic NHC ligands where the formation of dense hydrogen-bonded water clusters is promoted by the hydrophobic micro-environment of the polymer. The peak deconvolution at −2.0 V showed that strongly H-bonded water accounted for ∼92% on P5, compared with 41% on Au, suggesting that interfacial water was highly structured with strong intermolecular hydrogen bonding, thereby suppressing the HER. Additional upward peaks at 2938 and 2848 cm^{-1}, corresponding to the C–H stretching of P5, became more pronounced with increasing negative potentials, suggesting electrostatic attraction of the cationic polymer toward the electrode surface. A new peak at 1386 cm^{-1}, corresponding to symmetric stretching of hydrated bicarbonate, also appeared under cathodic bias, along with peaks between 1000 and 1200 cm^{-1} from bicarbonate hydration clusters. This peak intensity similarly increased with the negative bias, suggesting that the positively charged quaternary ammonium groups of P5 draw bicarbonate counterions toward the interface. Thus, the polymer ligands reorganized the interfacial environment by preconcentrating bicarbonate ions and structuring interfacial water, thereby enhancing CO_2 accessibility and suppressing the HER, collectively improving CO_2 reduction selectivity.

11864 | *J. Mater. Chem. A*, 2026, 14, 11848–11879

This journal is © The Royal Society of Chemistry 2026

Polycations with different head groups can profoundly influence the interfacial environment and product distribution in the eCO$_2$RR by simultaneously tuning local hydrophobicity and ion transport. Recent studies systematically examined this effect using hydrophobic *para*-terphenyl-trifluoroheptan-2-one copolymers (*p*TPN) functionalized with six distinct quaternary ammoniums on the side chains, including tri-methylammonium (TMA$^+$), piperidinium (Pip$^+$), pyridinium (Py$^+$), 1-methyl-imidazolium (Meim$^+$), 1-*n*-hexyl-imidazolium

(Hexim$^+$), and 1-methyl-benzimidazolium (Beim$^+$) (Fig. 11a).[154] These polymer ligands were mixed with commercial CuNPs (30–50 nm) and dropped on glassy carbon as the working electrode for the eCO$_2$RR in a H-cell with 0.1 M KHCO$_3$ (Fig. 11b). The results indicated that *p*TPN–TMA$^+$ and Pip$^+$ had a high H$_2$ FE of ~40% and ~50%, respectively. *p*TPN–Py$^+$ enhanced the CO$_2$ selectivity up to ~54% at −1.2 V, while the H$_2$ FE is still over 40%. For *p*TPN–Meim$^+$, the H$_2$ selectivity was as high as 80% at −1.2 V. On increasing the hydrophobicity at the N3 position
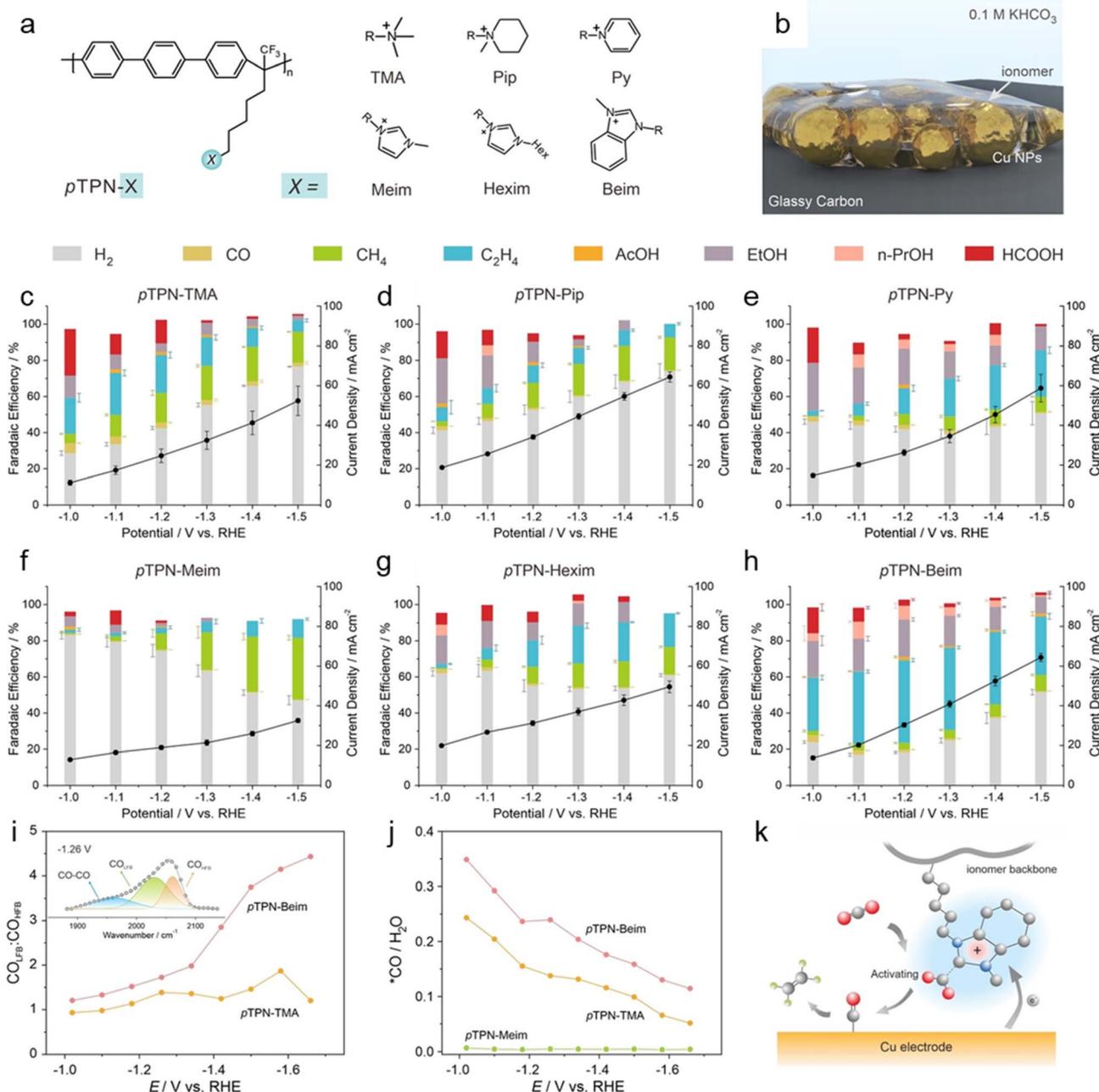
Fig. 11 (a) Structural illustration of *p*TPN–X ionomers. (b) Scheme of the *p*TPN–X-modified Cu electrode (Cu/*p*TPN–X) for the eCO$_2$RR. (c)–(h) Product distribution and current densities over the Cu/*p*TPN–X electrodes. (i) Ratios of *CO$_{LFB}$ to *CO$_{HFB}$ band intensity against the applied potentials. The inset shows typical peak decomposition of the ATR-SEIRAS acquired on Cu/*p*TPN–Beim at −1.26 V. (j) Ratios of ν(*CO$_L$) to ν(H$_2$O) band intensity against the applied potentials. (k) Schematic illustration of the Beim+ cation-enhanced CO$_2$RR toward C$_2$H$_4$ production. Reproduced with permission.[154] Copyright 2023 Wiley.

This journal is © The Royal Society of Chemistry 2026

J. Mater. Chem. A, 2026, **14**, 11848–11879 | **11865**

(*i.e.*, *p*TPN–Hexim$^+$), the H_2 FE decreased to ~55% at −1.2 V. For *p*TPN–Beim$^+$, the H_2 FE was significantly inhibited to ~16% and the overall C_{2+} product selectivity was high at 75.9% at −1.2 V (Fig. 11c–h). Cyclic voltammetry in nonaqueous electrolytes with dissolved R_4N^+ cations showed that (i) reduced peak currents increased in the presence of Py$^+$, Beim$^+$ and Meim$^+$ and (ii) the imidazolium cations improved CO_2 reduction kinetics as compared to Py$^+$. ATR-SEIRAS was used to obtain the details of surface species during the CO_2 reduction by the *p*TPN–Beim$^+$ modified Cu electrode. A vibrational peak at ~1666 cm^{-1} was assigned to the chemically bound carboxylate CO_2^- as the Beim–CO_2^- adduct, and another peak for the vibration band at around 1758 cm^{-1} arose from bound *COOH, by further protonation of Beim–CO_2^-. Both the linear-bonded *CO_L at

2100–1960 cm^{-1} and bridge-bonded *CO_B at ~1830 cm^{-1} were detected on *p*TPN–Beim$^+$ with a high coverage (Fig. 11i), as compared with other ammoniums. In addition, the ratio of ν(*CO_L) to ν(H_2O) band intensity of *p*TPN–Beim$^+$ was also higher than that of *p*TPN–TMA$^+$ and *p*TPN–Meim$^+$ (Fig. 11j), allowing C–C bond coupling to C_{2+} products. Therefore, *p*TPN–Beim$^+$ improved the conversion of CO_2 to *CO and high *CO coverage with multiple (strongly) adsorbed *CO species, leading to high C_{2+} selectivity by *CO dimerization (Fig. 11k). Meanwhile, the hydrophobicity of the Beim$^+$ cation disfavored the adsorption of water at the electrode–electrolyte interface.

The charge density of polycations also played an important role in the selectivity of the eCO$_2$RR. Andrew's group prepared ionic polymers with quaternary ammoniums through post-
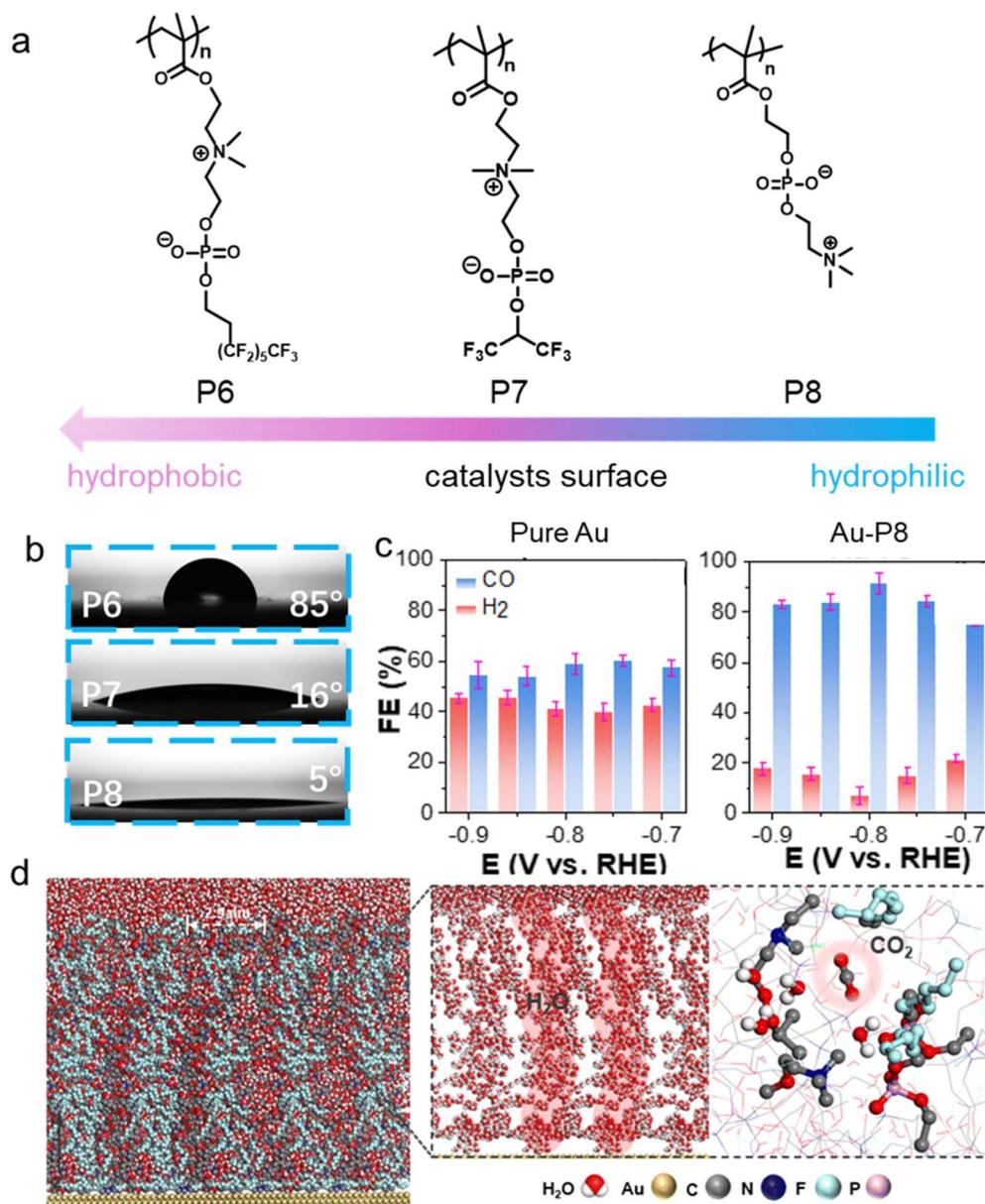

Fig. 12 (a) Chemical structures of zwitterion polymers: P6–P8. (b) Water contact angles of P6–P8 coated surfaces. (c) CO and H_2 FE of Au and Au–P6. (d) MD simulation of a representative system configuration (left) and zoomed-in area of water distribution and the solvated CO_2 molecule (right). Reproduced with permission.[156] Copyright 2024 The Royal Society of Chemistry.

11866 | *J. Mater. Chem. A*, 2026, **14**, 11848–11879

This journal is © The Royal Society of Chemistry 2026

functionalizing poly(pentafluorophenyl acrylate)$_{100}$ using N-boc-1,6-hexanediamine, followed by acid deprotection (PAM-1).[155] Ammonium-containing copolymers PAM-2 (35% methylation), PAM-3 (65% methylation) and PAM-4 (100% methylation) were prepared by methylating PAM-1 with methyl iodide. A higher ethylene FE was seen for Cu–PAM-1 with free amines and Cu–PAM-4 with 100% methylation. The pendant amine groups in PAM-1 are likely to promote ethylene formation by increasing the local basicity near the catalytic sites.

To balance CO_2 and proton transport, our group reported the use of hydrophobic zwitterions, e.g., fluorinated poly(2-methacryloyloxyethyl phosphoryl choline) (polyMPC, P6) for the eCO$_2$RR (Fig. 12a).[156] Compared with P8, the catalyst surface had a WCA of 85°, indicating a nearly perfectly balanced hydrophilicity-to-hydrophobicity (Fig. 12b). In the case of Au–P6, the J_{CO} is 3.6 times higher and n_{CO}/n_{H_2} is 9 times greater than those of Au/C at −0.9 V (Fig. 12c). The n_{CO}/n_{H_2} decreased to 3.5 (Au–P6) as fluorinated content decreased, showing that fluorinated groups are important for enhancing the CO_2-to-CO selectivity. Small angle X-ray scattering (SAXS) showed that P6 comprises branched cylinders and unstacking lamellae after fitting the scattering pattern with a combined cylindrical and lamellar model with a d-spacing of 2.9 nm. MD simulation revealed phase separation of ionic and fluorinated domains in P6, providing two pathways for mass transport of water and CO_2. Water molecules penetrate extensively into the zwitterionic channels, forming continuous hydrogen-bonded chains with an average hydrogen bonding density of 1.9. CO_2 preferentially associates with fluorinated tails, aligning oxygen atoms toward ammonium groups (Fig. 12d). This phase-separated microstructure improves mass transfer kinetics and enhances CO_2 reduction efficiency, achieving a 50–80% increase in FE and suppressing the HER.

Ionic polymers, depending on the content of ionic groups, are not stable in an aqueous solution. To prevent swelling, or potential dissolution during electrolysis, cross-linking may be essential to enhance mechanical robustness and chemical resistance. The cross-linked polyelectrolyte, while providing similar ionic transport control, forms a robust and stable interfacial layer that effectively immobilizes catalysts. Gu et al. used 1,6-diiodohexane to cross-link the copolymer of diallyldimethylammonium chloride and diallylmethylamine and obtained a cross-linked polyelectrolyte layer (c-PDDA) on the surface of metal catalysts.[157] Using AgNPs and InNPs as model catalysts, they studied the eCO$_2$RR performance under acidic conditions. c-PDDA coated AgNPs had the highest CO FE of 95 ± 3% at −1.57 V vs. the standard hydrogen electrode (SHE) at a current density of −100 mA cm^{-2}. The coated AgNPs were stable and retained a CO FE of >80% for electroreduction over 36 h at −200 mA cm^{-2}, while CO FE of bare AgNPs decreased by 52% after 10 h (43%) (Fig. 13a and b). For c-PDDA coated InNPs, the highest FE of formate was 76 ± 3% at −1.84 V vs. SHE at a current density of −200 mA cm^{-2}. Both uncoated AgNPs and InNPs primarily produce H_2, due to the high proton concentration in 0.1 M H_2SO_4 electrolyte (Fig. 13c and d).

To understand the underlying mechanism, a different polymer coated Ag micro-disk electrode (MDE) was used and the

simulation of generalized modified Poisson–Nernst–Planck (GMPNP) modeling was conducted. The HER polarization curves of Ag MDEs coated with c-PDDA, Sustainion XA-9, PTFE and Nafion D520 were collected in 10 mM of trifluoromethanesulfonic acid (HOTf). When coated with neutral PTFE, the plateau region is lower than that of the pure Ag MDE, indicating the limited diffusion coefficient of H^+ in PTFE. For cationic c-PDDA and Sustainion XA-9 coated Ag MDEs, the plateau current is lower than that of PTFE coated Ag. In particular, the c-PDDA coated Ag MDE had the lowest limiting current. The positively charged polymers therefore showed a suppression of the mass transport of H^+. Since the cation density of c-PDDA was 3 times that of Sustainion XA-9, the c-PDDA coating acted as the best layer to stop the diffusion of protons. The GMPNP results indicated that the migration rate of H^+ decreases with the increase of total charge density (ρ_p) of immobilized ionic sites (positively charged c-PDDA) and movable ions (cations). In addition, c-PDDA also changed the local pH near the cathode and the electric field strength in the Stern layer (E_{stern}). For c-PDDA, H^+ reduction can increase the local pH at the outer Helmholtz plane (OHP). Meanwhile, the CO_2 reduction generates OH^- that neutralizes H^+ and further increases local pH. For CO_2 reduction to CO, the single-electron reduction of CO_2 ($CO_2 + e^- \rightarrow CO_2^{\cdot-}$) is the rate determining step (RDS). As shown in Fig. 13e, the driving force of electron transfer from the cathode to CO_2 was from the potential difference between the cathode and OHP. With a higher E_{stern} in the presence of positively charged c-PDDA, the CO_2 reduction became favorable (Fig. 13f).

Cross-linked poly(ionic liquid) (PIL) coated metal catalysts can be obtained through in situ polymerization of ionic liquid monomers. For example, Xu et al. prepared poly(imidazolium–pyridine–imidazolium) coated CuNPs by adding CuNPs into imidazolium–pyridine–imidazolium. The PIL layer was formed by in situ radical polymerization and cross-linked by divinylbenzene (Fig. 14a).[158] The effect of counter ions on eCO$_2$RR performance was investigated in a flow cell that was equipped with a gas diffusion electrode (GDE) and anion exchange membrane (AEM). For CuNPs coated with PIL with F^- counter ions (Cu@PIL–F), the H_2 FE, CO FE, and $HCOO^-$ FE were 7.9%, 67.9% and 12.6% respectively. However, the H_2 FE of Cu@PIL with PF_6^- counter ions was 72.0%. The H_2 FE increased in the order of F^- (12.2%) < Cl^- (14.9%) < Br^- (24.4%) < I^- (39.9%) < BF_4^- (47.6%) < PF_6^- (72.0%) (Fig. 14b). The LSV curves indicate that Cu@PIL–F exhibits high catalytic activity for both the HER and eCO$_2$RR, with the eCO$_2$RR activity surpassing that of the HER, leading to a low H_2 FE. The CO_2-temperature programmed desorption (TPD) showed intense chemisorption peaks at over 300 °C and a broad strong physisorption bond at ~158 °C for Cu@PIL–F, indicating the enriched local CO_2 concentration at the interface, thereby improving its mass transport. The highest occupied molecular orbital (E_{HOMO}) of F^- was 2.103 eV and the number of electrons transferred from F^- to the cation was 0.756, whereas those of PF_6^- were −5.301 eV and 0.248. Therefore, F^- as a counter ion was considered to have higher electron-donating ability that facilitates the eCO$_2$RR, compared to other counter ions (Fig. 14c). In addition, imidazolium-
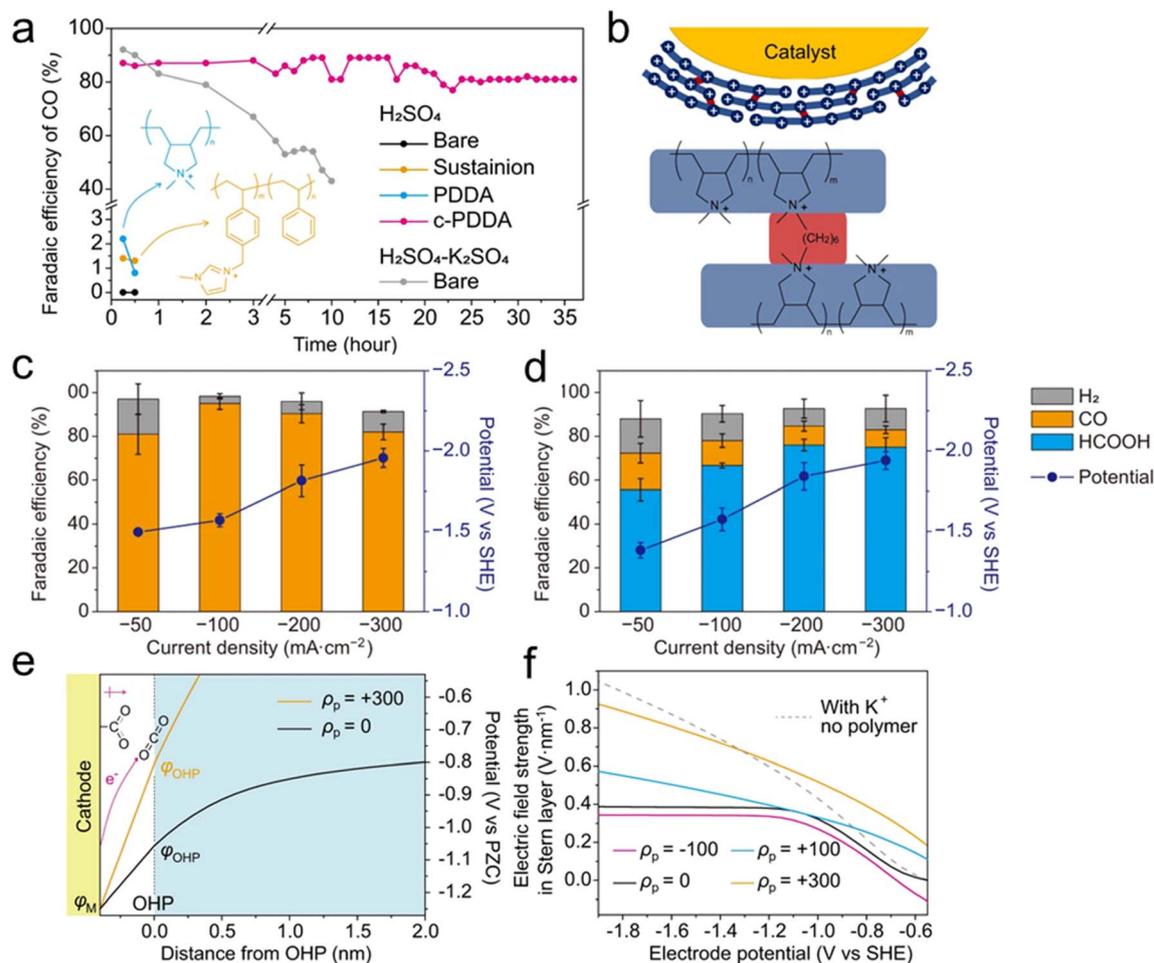
This journal is © The Royal Society of Chemistry 2026

J. Mater. Chem. A, 2026, **14**, 11848–11879 | **11867**

Fig. 13 (a) CO FE during electrolysis with a constant current density of -200 mA cm^{-2}. Bare Ag NPs (black), Sustainion XA-9 modified Ag NPs (orange), PDDA modified Ag NPs (blue) and c-PDDA modified Ag NPs (magenta). (b) Schematic of a c-PDDA modified catalyst. (c) and (d) H$_2$ FE (gray), CO FE (orange) and formic acid (blue), and the electrode potential (dark blue curves), while (c) Ag NPs and (d) In NPs were used as the catalysts. (e) Potential profiles on Ag electrodes covered by polymer layers with $\rho_p = 300$ C cm^{-3} (orange curve) and $\rho_p = 0$ (black curve) in 10 mM HOTf at -1.8 V vs. SHE. A schematic of the rate determining step of CO$_2$ reduction is shown. (f) Plots of the electric field strength in the Stern layer based on the electrode potential. Solid curves: Ag electrodes covered by polymer layers with different ρ_p values (unit: C cm^{-3}) in 10 mM HOTf. Gray dashed curve: a bare Ag electrode in 10 mM HOTf + 40 mM KOTf. Reproduced with permission.[157] Copyright 2023 Springer Nature.

containing PIL also enriched the local concentration of CO$_2$ through the formation of CO$_2$ adducts. Cu@PIL–Cu$_2$O hybrid catalysts with Cu$_2$O deposited on the surface of the PIL shell on Cu exhibited a high (C$_{2+}$) FE of 76.1% at -0.85 V.[159]

6. Porous polymer coated nanocatalysts for the eCO$_2$RR

Metal–organic frameworks (MOFs) and covalent organic frameworks (COFs), both of which have unique porous and crystalline architectures, have also emerged as highly promising materials for the electrochemical reduction of the eCO$_2$RR.[160–163] MOFs consist of metal ions or clusters coordinated with organic linkers, while COFs, in contrast, possess covalently linked, π-conjugated backbones rich in heteroatoms (e.g., N and S).[164–166] The periodic three-dimensional networks with ultrahigh surface areas (>1000 m^2 g^{-1}) and tunable pore sizes can enable efficient CO$_2$ adsorption/storage and control the mass transport

of CO$_2$/intermediates, potentially promoting deep reduction of CO$_2$.[167,168] The presence of catalytically active metal centers or single-atom sites within porous frameworks allows fine control over the binding energies and stabilization, providing structural robustness and facilitating charge transport.[169–173] Moreover, their tunable pore microenvironments allow precise control of local reaction conditions, such as electrode–electrolyte interactions and solvent effects, effectively enabling selective formation of CO$_2$ reduction products.[174–176]

To directly evaluate the impact of well-defined porous structures on tuning the local environment around the active sites, one can grow catalytically non-active MOFs on a catalytically active metal electrode. For example, Hod's group coated a thin layer of Zr$_6$-oxo based MOF (UiO-66) with a control thickness in the range of 0.5 to 1.8 μm on Ag foil.[177] Compared to pure foil, Ag coated with ~0.9 μm of UiO-66 showed a 43% increase in CO selectivity at -0.8 V. The enhancement was attributed to abundant defect sites in UiO-66, characterized as
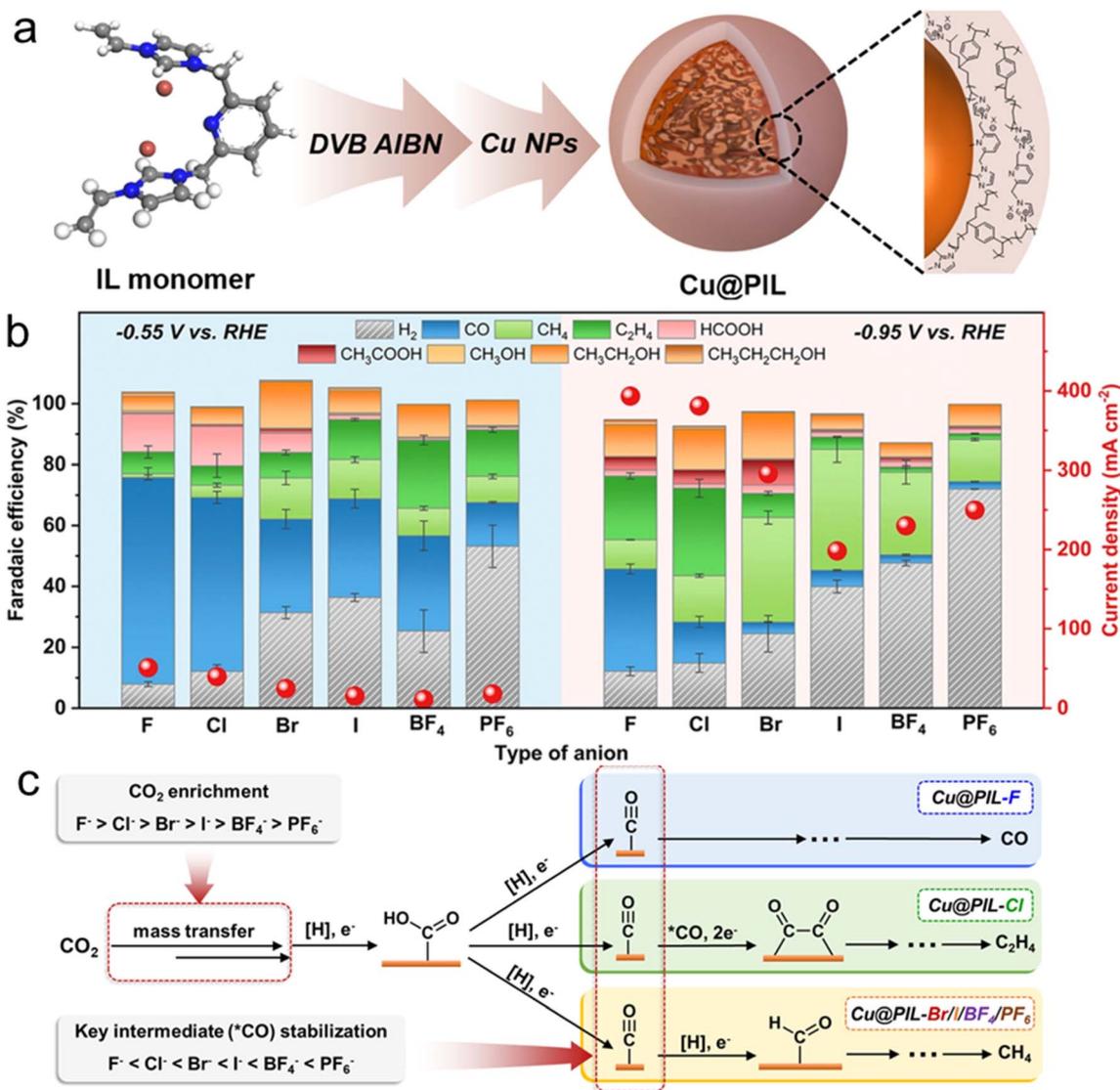
11868 | J. Mater. Chem. A, 2026, **14**, 11848–11879

This journal is © The Royal Society of Chemistry 2026

Fig. 14   (a) Schematic illustration for the structure of an IL monomer and the preparation of Cu@PIL. (b) eCO$_2$RR performance of Cu@PIL−X-1.2 with different anions (light blue area (left): at a cathodic potential of −0.55 V; light red area (right): at a cathodic potential of −0.95 V). (c) Proposed pathway of the Cu@PIL catalyzed eCO$_2$RR with different anions. Reproduced with permission.[158] Copyright 2021 Elsevier.

the Brønsted acid, Zr–OH. These acid sites promote CO$_2$ reduction by acting as proton sources which can stabilize the activated *COO$^-$ intermediates. To verify this mechanism, the adsorption and desorption of OH$^-$ as a probe were studied. The results indicated that the overpotential required for OH$^-$ absorption on UiO-66 coated electrodes was lower than that on the pure Ag electrode. Using benzoic acid to cap the OH sites on MOF surfaces, the CO FE of modified Ag–UiO-66 dropped by 21%. Similarly, they studied the impact of nitrile-functionalized UiO-66 (or UiO-66=CN) on a Bi electrode. Compared with pure Bi, the UiO-66–CN coating achieved an FE of HCOOH up to 93% and exhibited 7 times faster kinetics, due to the porous MOF acting as a CO$_2$ reservoir. Because of the high concentration of BA–CN groups, the local CO$_2$ concentration near the Bi catalyst increased to ∼0.82 M, which was ∼27-fold higher than that in the bulk electrolyte (∼0.030 M), as indirectly calculated from the

ATR-IRRAS at different CO$_2$ concentrations. In addition, the value was confirmed using quinone as a redox probe which reversibly binds with CO$_2$.[178]

To prepare MOF–NP or COF–NP composites, various synthetic strategies have been developed and were recently summarized in review papers.[179–183] In general, there are two straightforward methods. The first method is the "impregnation" where a MOF or COF powder is mixed with a solution containing metal precursors (or mixing them in the solid state), followed by the reduction inside (mostly) or on the external surface of the MOF or COF. The second is *in situ* growth of a MOF or COF on pre-synthesized NPs, leading to the encapsulation of NPs within the framework. In the latter case, embedding pre-synthesized NPs avoids disrupting a single lattice plane, whereas impregnation involves lattice distortion during NP growth.

This journal is © The Royal Society of Chemistry 2026

J. Mater. Chem. A, 2026, 14, 11848–11879 | 11869

Cu₂O@MOF on Cu foil (Cu₂O@MOF–CF) was prepared by heating a mixture of CuSO₄·5H₂O, 1,3,5-tris(1-imidazolyl) benzene and 4,4′-biphenyldicarboxylic acid with NaOH activated Cu foil.[184] The C_2H_4 FE of Cu₂O@MOF–CF was 48.6% at −1.11 V, about 2.2 times that for pure Cu foil. The enhanced ethylene selectivity was attributed to the surface Cu₂O, which generated more *CO intermediates, leading to a high *CO coverage on the Cu foil and facilitating C–C coupling of C_2H_4. As confirmed using DFT calculations, Cu₂O@MOF showed a lower free energy for the first electron transfer step and weaker CO adsorption energy. Cu₂O@MOF–CF also exhibited 70 times greater surface area, compared to pure Cu foil, indicating that porous Cu₂O@MOF provided more active sites for CO_2 activation. In a more recent study, Cu@MOF prepared on Cu foil through microwave synthesis was reported with higher selectivity to C_2H_4 by Zhang et al.[185] Interestingly, Cu@MOF converted to Cu nanocubes during electrolysis, and its FE of C_2H_4 was 49.6%, much higher than that of Cu foil (∼25% of C_2H_4 FE). The coating of MOF on the catalytic metal also provided a local electric field that improved the adsorption energy of *CO. The growth of oriented NiCu–MOF nanorod arrays on Cu₂O

(Cu₂O@MOF/CF) via solvothermal synthesis improved the ethanol selectivity by 44.3% at −0.615 V.[186] DFT calculations indicated that internal electric field polarization between Cu₂O and NiCu–MOF, resulting from the asymmetric electron distribution, enhanced the adsorption of *CO and enabled C–C coupling. Similarly, atomically dispersed Co^{2+} in a COF by mixing CoCl₂ with a redox-active COF achieved ∼66.8% ethanol FE at −2.87 mA cm⁻².[187] The reversible variation in the oxidation state of Co^{2+} endowed the catalyst with high stability. A ∼20% current loss is observed, and FE ethanol remains at ∼60% after electrolysis at −0.67 V over 24 h.

A more structurally conservative yet highly effective strategy to enhance the catalytic performance of MOFs is the incorporation of strong coordinating ligands into their frameworks. This approach preserves the intrinsic crystallinity and porosity of the MOF while introducing well-defined coordination environments capable of stabilizing active metal centers. After the formation of the MOF skeleton, catalytic metal ions or nanoclusters can be precisely encapsulated through coordination interactions, enabling atomic-level control over the geometry and electronic structure of active sites. Chen et al. demonstrated
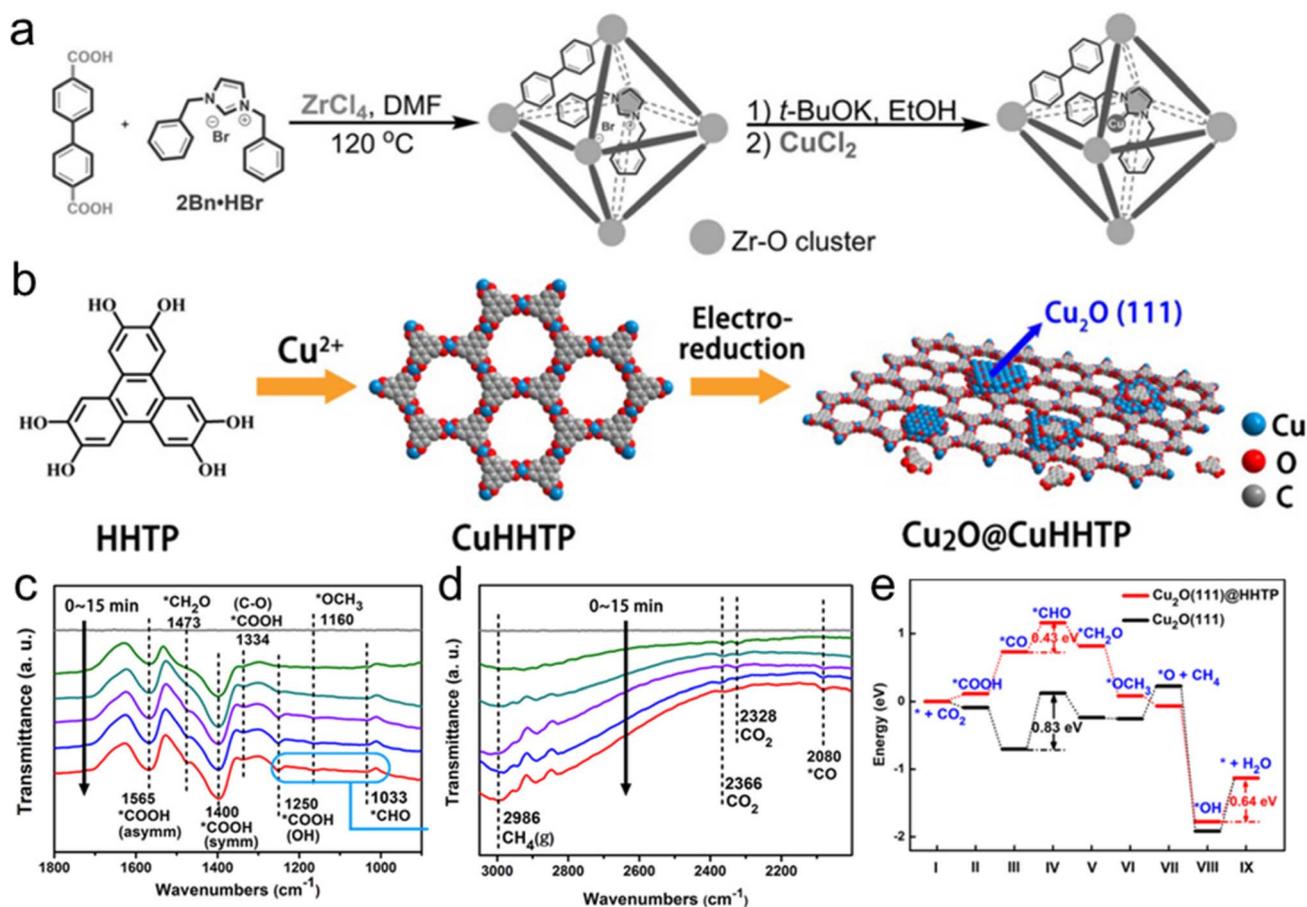

Fig. 15 (a) Synthetic scheme of 2Bn−Cu@UiO-67. Reproduced with permission.[188] Copyright 2021 Wiley. (b) Solvothermal synthesis of CuHHTP and preparation of Cu₂O@CuHHTP via electrochemical treatment of CuHHTP at −1.2 V for 30 min. (c and d) Operando ATR-FTIR spectra on Cu₂O@CuHHTP collected at −1.4 V vs. RHE in CO_2 saturated 0.1 M KCl/0.1 M KHCO₃ electrolyte. (e) Free-energy diagrams of the eCO₂RR to CH₄ for Cu₂O-(111)@HHTP (red line) and the pristine Cu₂O (111) crystal plane (black line). Reproduced with permission.[190] Copyright 2020 Wiley.

11870 | J. Mater. Chem. A, 2026, 14, 11848–11879

This journal is © The Royal Society of Chemistry 2026

the synthesis of Cu-containing Zr-based UiO-67 by incorporating a NHC precursor, dibenzyl imidazolium, during solvothermal synthesis of MOF. Afterwards, $CuCl_2$ was introduced under alkaline conditions. NHC–Cu was produced within the pores as 2Bn–Cu@UiO-67 (Fig. 15a).[188] The CH_4 FE of 2Bn–Cu@UiO-67 reached 81% at −1.4 V. DFT simulation suggested charge transfer from NHC to the Cu stabilized *CO on the Cu site, promoting further hydrogenation. This aligned with infrared spectroscopy studies on the formation of *OCH_3 at 1110 cm^{-1} with 2Bn–Cu@UiO-67. Similarly, the imidazolium carboxylate functionalized NHC-based COF (NHC–CO_2–COF) was demonstrated to prepare metal–NHC@COF under mild conditions.[189]

Cu_2O–MOF hybrid catalysts provide an excellent example of how MOF-based systems can tune product selectivity. CH_4 is thermodynamically favored on Cu due to its low reduction barrier (−0.24 V at pH 7). However, high CH_4 selectivity faces a kinetic disadvantage because of eight-electron transfer and the formation of multiple products from different facets of the nanocatalysts. On a conductive copper-based MOF (CuHHTP), Cu_2O could be synthesized through in situ electroreduction. After 30 minutes of electroreduction, Cu_2O NPs with an average size of ca. 3.5 nm grow uniformly on CuHHTP, where periodically distributed CuO_4 nodes would be expected (Fig. 15b).[190] Cu_2O when supported on conductive carbon black ($Cu_2O@CCB$) and commercial Cu_2O showed a CH_4 FE of 30% and 15%, respectively. $Cu_2O@CuHHTP$ was highly selective to CH_4 with a FE of 73% at −1.4 V owing to the highly exposed Cu_2O (111) single lattice plane. ATR-FTIR showed the peaks corresponding to key intermediates for CO_2 hydrogenation: 1250 cm^{-1}, 1334 cm^{-1}, 1400 cm^{-1}, and 1565 cm^{-1}, corresponding to the OH deformation, C–O stretch, symmetric stretch, and asymmetric stretch of the *COOH intermediate, respectively (Fig. 15c). Meanwhile, the peak at 2080 cm^{-1}, corresponding to the *CO intermediate, was blue shifted relative to the reported value (~2065 cm^{-1}), probably due to the hydrogen bonding between *CO and the hydroxyl group of HTTP (Fig. 15d). DFT simulation indicated that CO_2 was absorbed on Cu_2O (111) and converted to *COOH, and all key intermediates, e.g., *CHO, *CH_2O and *OCH_3, were stabilized by hydrogen bonding with HHTP. The free energy diagram (Fig. 15e) highlighted the key transition step from *CO to *CHO where the free energy barrier decreases from 0.83 eV to 0.43 eV in the presence of HHTP. Similarly, Cu@THQ consisting of tetrahydroxy-1,4-quinone (THQ) with square-planar CuO_4 nodes had a similar 2-D conductive network. Upon reduction, the formation of metallic Cu (5.5 nm) instead of Cu_2O was selective to C_2H_4 with an FE of 42%.[191]

The MOF also influenced the formation of NPs during the reduction of metal precursors via impregnation. For example, Hwang's group studied the formation of Pd and AuPd bimetallic NPs through in situ (co)reduction of $Pd(NO_3)_2$ and $HAuCl_4$ within Zr–MOF-808.[192] Under significant local tensile strain provided by the MOF skeletons, the lattice expansion of Pd (with or without Au) was as large as ~2.6%, compared to that of Pd/C. This tensile strain had a pronounced influence on catalytic behavior by weakening the adsorption of *CO species. The

eCO_2RR efficiency of Pd and AuPd bimetallic NPs was significantly higher than that of Pd/C. The FE of formate for MOF–Pd and MOF–AuPd was 90% and 99%, respectively.

COFs, on the other hand, often have extended π-conjugated skeletons and abundant N sites to promote electron delocalization, particularly attractive as the catalyst support for the eCO_2RR.[193,194] The COF prepared from 2,3,9,10,16,17,23,24-octahydroxyphthalocyaninato copper (CuPc–8OH) could support the growth of Cu nanoclusters (Cu–NC@CuPc–COF) through impregnation of Cu^{2+} and in situ reduction with hydrazine.[195] The nanoconfinement provided by the nanochannels in the COFs limited the overgrowth of Cu, resulting in Cu nanoclusters with 1.2 nm. The conductivity of Cu–NC@CuPc–COF contributed largely to its high partial current density, i.e., 538 mA cm^{-2} at −1.2 V with CH_4 FE up to 60%. A unique advantage of COFs lies in their ability to mediate ion transport through cation–π interactions. Such interaction can guide ion accumulation along specific channels and change the local availability of protons/hydroxides. A recent study by Ozden et al. demonstrated this concept by constructing a bulk heterojunction on catalysts by coating hydrophobic Hex–Aza–COF on CuNPs. The resulting hybrid achieved a remarkable energy efficiency (EE) towards C_{2+} of 18% at a $J_{C_{2+}}$ of 127 mA cm^{-2}.[196] In a membrane electrode assembly (MEA) electrolyzer, the accumulation of cations (K^+) on the surface of the cathode can significantly limit the CO adsorption and consequently promotes the HER. With COF coating, the diffusion of K^+ was slowed down by three-orders of magnitude. DFT calculations indicate that the hydrophobic COFs constrict K^+ migration while enhancing OH^- adsorption, facilitating C–C coupling. Similarly, Shao and co-workers demonstrated that Cu single atoms or nanoclusters grown in the COF made of 2,6-diaminoanthraquinone(DAAQ) and 2,4,6-triformylphloroglucinol (TFP) have selectivity for the eCO_2RR to CH_4.[197] Cu nanoclusters in DAAQ–TFP–COF had an FE of CH_4 of about 56% at −1.26 V. The DFT results suggested that the C=O groups of DAAQ–TFP coordinated with K^+ cations, which largely suppressed the surface adsorption of water. Similarly, Cao et al. encapsulated Cu nanoclusters into NiPc–COF by dispersing Cu_{32} clusters on NiPc–COF, where Cu promotes C–C coupling while porous COF provides a high CO_2 adsorption of 16.8 cm^3 g^{-1}.[198] A (C_{2+}) FE of 57.1% was achieved with a current density of 353.3 mA cm^{-2} at −1.6 V. In addition to Cu nanoclusters, other metal clusters and single-atom catalysts have been shown to exploit COF channel confinement to regulate mass transport and the electronic structure, thereby enhancing eCO_2RR efficiency.[199–201]

COF ionomers, prepared by chemically linking building blocks containing multiple ionic groups,[202–205] can benefit from both the porosity and local electric field. For example, a catalyst ink was prepared by physically mixing commercial CuNPs with a sulfonated 2D COF ionic nanosheet (NUS9).[203] The porous COF backbone with a high density of ionic groups enhanced the local concentration of CO_2 and K^+, promoted the dissociation of H_2O, mitigated the *CO coverage on the catalyst surface, and lowered the rate determining step (RDS) for CH_4 production (i.e., *CO + *H → *CHO). A prominent CH_4 FE of 66% in an acid electrolyte (0.5 M K_2SO_4, pH = 2) was obtained. Meanwhile, the

This journal is © The Royal Society of Chemistry 2026

J. Mater. Chem. A, 2026, 14, 11848–11879 | 11871

operation time exceeded 9 h at 200 mA cm^{-2}. In another example reported by Guo et al., a quaternary ammonium salt (N(CH$_3$)$_4$Br) was loaded into hydrophobic COF (Me–COF) pre-modified with fluorine.[204] Due to the strong affinity between quaternary ammonium cations and bicarbonate, Me–COF showed a high CO$_2$ adsorption capacity than bare COF. The C$_2$H$_4$ FE increased from ~18% to 36% at 200 mA cm^{-2} after modifying the Cu electrode with Me–COF. In practical alkaline zero-gap MEA devices, the C$_2$H$_4$ FE reached 46.6% at 500 mA cm^{-2} with a cell voltage of 3.61 V. In situ ATR-SEIRAS and Raman spectroscopy suggested that Cu/Me–COF had a higher surface coverage with the *CO intermediate and favored *CO dimerization. The ν(*CO$_L$)/ν(H$_2$O) area ratio for the Cu/Me–COF electrode was noticeably higher than that for pure Cu. The *CO adsorption energies from DFT on Cu (100) and Cu (100)/Me–COF were calculated to be −1.12 eV and −1.33 eV, respectively, indicating stronger *CO adsorption on the Cu (100)/Me–COF electrode.

The key challenge in using MOF–NP or COF–NP composites for the eCO$_2$RR is their intrinsically poor conductivity. Most MOFs are constructed from metal nodes bridged by organic linkers (non-conductive), which, although structurally crystalline and porous, typically provide limited electron conductivity. As a result, when MOF–NP composites are coated onto an electrode surface, only a small fraction of the embedded catalytic metal sites is electrochemically accessible, while the majority remains electronically isolated within the insulating MOF matrix. One solution is to convert the organic framework to carbon through calcination. Such MOF-derived composites then became NPs encapsulated in a conductive carbon network. This sacrifices the structural periodicity of MOFs, but those hybrid catalysts have proven to be extremely active in the eCO$_2$RR.[206–210] For example, Sun et al. synthesized a carbon encapsulated copper-doped cerium oxide composite (Cu/CeO$_2$@C) by one-pot pyrolysis of MOF precursors (Fig. 16a).[211] In a flow cell, Cu/CeO$_2$@C had a selectivity to CH$_4$ of 80.3% at −1.5 V while that of Cu/CeO$_2$ is 59.2% (Fig. 16b). Carbon played an important role in enhancing the conductivity of Cu/CeO$_2$ and promoting electron transfer. Cu/CeO$_2$@C had a lower charge-transfer reactance (R_{ct}) of ~9 Ω measured from Nyquist plots, as compared to Cu/CeO$_2$ (~14 Ω) (Fig. 16c), indicating higher charge transfer and kinetics. In addition, Cu/CeO$_2$@C showed higher CH$_4$ partial current density (J_{CH_4}, 138.6 mA cm^{-2}) than Cu/CeO$_2$ (J_{CH_4}, 81.5 mA cm^{-2}) at −1.5 V. Similarly, a HKUST-1 embedded paddle-wheel Cu dimer by pyrolysis had a C$_2$H$_4$ FE of 45% at −1.5 V.[212]

Alternatively, if metal NPs are interconnected to form a conductive network, it would allow the efficient delivery of electrons for electroreduction. As demonstrated by Peng et al.,[213] PCN-222(Cu) MOF prepared from tetrakis(4-carboxyphenyl)porphyrin Cu was first impregnated with chloroauric acid that was further reduced under basic conditions. Au nanoneedles (AuNNs) with an average diameter of 10 nm were formed in alignment with the MOF pore channels.
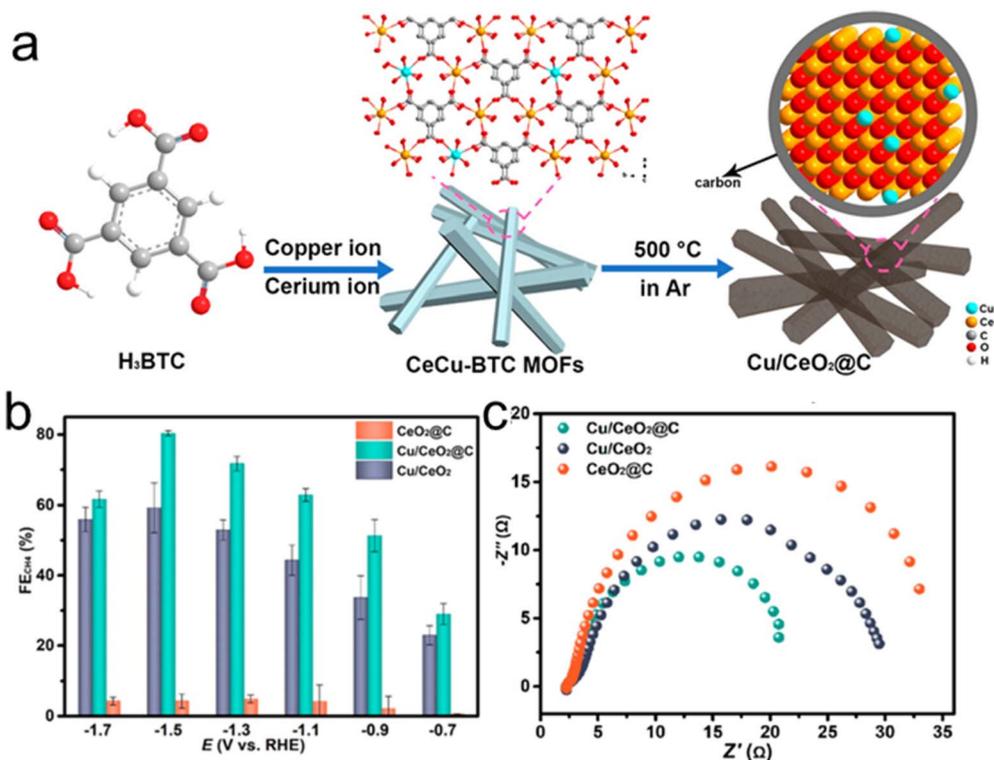

Fig. 16 (a) Schematic illustration for the synthesis of Cu/CeO$_2$@C. (b) Product FE of Cu/CeO$_2$@C at varied applied potentials. (b) The comparison of CH$_4$ selectivity. (c) Nyquist plots of Cu/CeO$_2$@C, Cu/CeO$_2$ and CeO$_2$@C. Reproduced with permission.[211] Copyright 2023 American Chemical Society.

11872 | J. Mater. Chem. A, 2026, 14, 11848–11879

This journal is © The Royal Society of Chemistry 2026

AuNN@PCN-222(Cu) had a high FE of 52.5% of C_2H_4 at -1.2 V. As a control, scattered AuNPs formed within PCN-222(Cu) (AuNP@PCN-222(Cu)) obtained by chemical reduction under neutral conditions exhibited only ~25% C_2H_4 FE at -1.2 V. *In situ* ATR-SEIRAS of AuNN@PCN-222(Cu) suggested a decreased peak at 2108 cm^{-1} and an increased peak at 1750 cm^{-1} with the increase of potentials, assigned to *CO adsorbed on AuNNs and *CHO intermediates adsorbed on the metalloporphyrins. DFT calculations suggested that the reaction mechanism likely proceeds *via* a tandem pathway: CO is first generated on the impregnated Au nanoneedles, and these CO species subsequently coupled with *CHO intermediates adsorbed on the metalloporphyrins to produce C_2H_4.

7. Summary and outlook

In this review, we have summarized recent advances in nanocatalysts modified with polymer ligands for the eCO$_2$RR, encompassing hydrophobic, conductive, ionic, and porous polymer systems. The highlighted studies collectively reveal emerging insights into how ligand chemistry governs catalytic behavior at the catalyst–electrolyte interface, potentially offering a molecular-level understanding of how interfacial engineering can enhance reactivity. The key enhancement mechanisms center around microenvironmental control, *e.g.*, the solvation structure, local CO_2 concentration, electronic structures and mass transport of ions/water, all of which create more favorable conditions for CO_2 activation and intermediate stabilization. These findings can power the next-generation design of ligands as a strategic tool to accelerate the discovery of new catalysts in eCO$_2$RR systems. Despite these advances, significant challenges remain in achieving precise control over polymer–catalyst interactions, dynamic interfacial behavior, and real-time characterization under *operando* conditions. In particular, the inherently dynamic nature of polymer-metal interfaces under bias presents fundamental challenges for establishing clear structure–function relationships in the eCO$_2$RR.

First of all, selective surface modification of metal nanocatalysts is being overlooked currently. The reactivity of nanocatalysts is intrinsically governed by their surface energy and atomic arrangement, as determined by the exposed crystal facets. For example, CH_4 formation is favored on Cu (111) facets, whereas C_2H_4 formation occurs on Cu (100) facets.[214] The CO generation rate is 20 times higher when Pb is deposited on Au (211) than on Au (100).[215] Hence, selectively adding polymer ligands to specific facets of nanocatalysts is a viable strategy to enhance product selectivity and the reaction rate. By designing polymers with tailored functional groups or competitive ligands,[216] it becomes possible to selectively adsorb them onto specific crystal planes. Ultimately, facet-selective polymer modification allows for "on demand" opening of the surface for catalysts, providing new pathways for rational design of nanocatalysts in the eCO$_2$RR.

Second, new ligand chemistry is underdeveloped. While strong coordination between ligands and metal surfaces is generally desirable, we and others have shown that even ligands with robust coordination motifs, *e.g.*, NHCs, underwent partial desorption at reductive potentials.[111,217] For example, NHCs bound to Au exhibit excellent stability within moderate potential windows, yet their electrochemical stability typically breaks down below approximately -0.8 V.[217] This limitation is acceptable for noble metal catalysts like Au and Ag but insufficient for less active Cu-based catalysts, which commonly operate below -1.0 V during the eCO$_2$RR. Pursuing ever-stronger covalent coordination alone may not fully resolve the trade-off between stability and accessibility of catalytic sites. Instead, a promising direction is the development of polymer ligands capable of dynamic exchange on the surface, allowing reversible desorption and adsorption under electrolysis.[218] This dynamic exchange also provides the possibility to construct polymer–metal interfaces that combine long-term structural robustness. Meanwhile, ligand desorption, chemical degradation (on the extended polymer chains, not limited to the binding motifs), and mechanical reorganization during extended electrolysis remain largely unexplored, highlighting the need for systematic studies on polymer durability and aging under realistic eCO$_2$RR operating conditions.

Third, most polymer ligands are catalytically inert, serving primarily as non-catalytic stabilizers rather than as active components in the eCO$_2$RR. Introducing catalytically active motifs into polymer backbones possibly offers an emerging strategy to bridge molecular catalysis and nanocatalysis. Organic amines or ammonium groups, such as pyridine[219,220] and imidazolium derivatives,[221] have been shown to act as metal-free CO_2 reduction catalysts through reversible dearomatization/aromatization cycles. By incorporating these functional moieties into polymer frameworks, it becomes possible to construct hybrid catalytic interfaces where both the polymer and metal centers cooperatively participate in CO_2 activation.[222,223] The organic functional groups can serve as co-catalytic sites, pre-activating or even capturing CO_2.[224] A more rational design of redox-active and catalytically functional polymer ligands is promising to couple cascaded CO_2 direct capture from air and subsequent reduction.

Lastly, the development and application of advanced *in situ* characterization tools are crucial for elucidating the role of polymer ligands in the eCO$_2$RR. At present, techniques such as ATR-SEIRAS and *in situ* Raman spectroscopy as spectroelectrochemistry tools provide valuable insights into the electronic structure and the evolution of surface species. However, these methods do not fully capture the dynamic switch of polymer chains and their solvation. There is a need to develop approaches that combine *in situ* spectroscopy with complementary imaging and scattering techniques to observe dynamic processes and monitor dynamic changes at the catalyst–polymer interface. For example, neutron scattering, which is sensitive to hydrogen atoms, when coupled with electrochemistry, can resolve the solvation of ligand layers and provide insights into the hydrogen bonding networks of water. *In situ* imaging techniques, *e.g.*, electrochemical-transmission electron microscopy (EC-TEM) in a liquid cell, can capture dynamic surface changes, potentially correlated with ligand–metal coordination environment change. Coupling these *operando*

This journal is © The Royal Society of Chemistry 2026

J. Mater. Chem. A, 2026, **14**, 11848–11879 | **11873**

measurements with multiscale computational approaches, including molecular dynamics and first-principles simulations, will be essential for quantitatively linking polymer dynamics to catalytic performance.

Conflicts of interest

There are no conflicts to declare.

Data availability

No primary research results, software or code have been included, and no new data were generated or analyzed as part of this review.

Acknowledgements

References

1 L. Liu and A. Corma, *Chem. Rev.*, 2018, **118**, 4981–5079.

2 P. Prinsen and R. Luque, in *Nanoparticle Design and Characterization for Catalytic Applications in Sustainable Chemistry*, ed. R. Luque and P. Prinsen, The Royal Society of Chemistry, 2019, DOI: 10.1039/9781788016292-00001.

3 C. Xie, Z. Niu, D. Kim, M. Li and P. Yang, *Chem. Rev.*, 2020, **120**, 1184–1249.

4 S. Cao, F. Tao, Y. Tang, Y. Li and J. Yu, *Chem. Soc. Rev.*, 2016, **45**, 4747–4765.

5 M. Muzzio, J. Li, Z. Yin, I. M. Delahunty, J. Xie and S. Sun, *Nanoscale*, 2019, **11**, 18946–18967.

6 H. Y. Younan Xia and C. T. Campbell, *Acc. Chem. Res.*, 2013, **46**, 1671–1672.

7 H. Zhang, M. Jin, Y. Xiong, B. Lim and Y. Xia, *Acc. Chem. Res.*, 2013, **46**, 1783–1794.

8 L. Jin, S. Thanneeru, D. Cintron and J. He, *ChemCatChem*, 2020, **12**, 5932–5937.

9 L. Jin, B. Liu, S. S. Duay and J. He, *Catalysts*, 2017, **7**, 44.

10 H. Guan, C. Harris and S. Sun, *Acc. Chem. Res.*, 2023, **56**, 1591–1601.

11 L. Lu, S. Zou and B. Fang, *ACS Catal.*, 2021, **11**, 6020–6058.

12 A. H. Jenkins and J. W. Medlin, *Acc. Chem. Res.*, 2021, **54**, 4080–4090.

13 P. D. Coan, C. A. Farberow, M. B. Griffin and J. W. Medlin, *ACS Catal.*, 2021, **11**, 3730–3739.

14 Y. Kim, S. Ji and J.-M. Nam, *Acc. Chem. Res.*, 2023, **56**, 2139–2150.

15 S. Kango, S. Kalia, A. Celli, J. Njuguna, Y. Habibi and R. Kumar, *Prog. Polym. Sci.*, 2013, **38**, 1232–1261.

16 Z. B. Shifrina, V. G. Matveeva and L. M. Bronstein, *Chem. Rev.*, 2020, **120**, 1350–1396.

17 K. R. Kahsar, D. K. Schwartz and J. W. Medlin, *J. Am. Chem. Soc.*, 2014, **136**, 520–526.

18 C. A. Schoenbaum, D. K. Schwartz and J. W. Medlin, *J. Catal.*, 2013, **303**, 92–99.

19 C.-H. Lien and J. W. Medlin, *J. Catal.*, 2016, **339**, 38–46.

20 C. Majumder, *Langmuir*, 2008, **24**, 10838–10842.

21 Z. Cao, J. S. Derrick, J. Xu, R. Gao, M. Gong, E. M. Nichols, P. T. Smith, X. Liu, X. Wen and C. J. A. C. Copéret, *Angew. Chem., Int. Ed.*, 2018, **130**, 5075–5079.

22 H. Tsunoyama, N. Ichikuni, H. Sakurai and T. Tsukuda, *J. Am. Chem. Soc.*, 2009, **131**, 7086–7093.

23 P. Liu and J. K. Nørskov, *Phys. Chem. Chem. Phys.*, 2001, **3**, 3814–3818.

24 S. H. Pang, C. A. Schoenbaum, D. K. Schwartz and J. W. Medlin, *Nat. Commun.*, 2013, **4**, 2448.

25 G. Chen, C. Xu, X. Huang, J. Ye, L. Gu, G. Li, Z. Tang, B. Wu, H. Yang, Z. Zhao, Z. Zhou, G. Fu and N. Zheng, *Nat. Mater.*, 2016, **15**, 564–569.

26 S. Solomon, G.-K. Plattner, R. Knutti and P. Friedlingstein, *Proc. Natl. Acad. Sci. U. S. A.*, 2009, **106**, 1704–1709.

27 A. A. Lacis, G. A. Schmidt, D. Rind and R. A. Ruedy, *Science*, 2010, **330**, 356–359.

28 S. Akrami, Y. Murakami, M. Watanabe, T. Ishihara, M. Arita, M. Fuji and K. Edalati, *Appl. Catal., B*, 2022, **303**, 120896.

29 C. D. Koolen, W. Luo and A. Züttel, *ACS Catal.*, 2023, **13**, 948–973.

30 H. Zhao, X. Liu, C. Zeng, W. Liu and L. Tan, *J. Am. Chem. Soc.*, 2024, **146**, 23649–23662.

31 Z. Zhang, Y. Li, Y. Huang, H. Cheng, Y. Zhao, Z. Li, Y. Hou, L. Lei and B. Yang, *Electrochem. Commun.*, 2023, **152**, 107519.

32 Z. Sun, T. Ma, H. Tao, Q. Fan and B. Han, *Chem*, 2017, **3**, 560–587.

33 M. G. Kibria, J. P. Edwards, C. M. Gabardo, C.-T. Dinh, A. Seifitokaldani, D. Sinton and E. H. Sargent, *Adv. Mater.*, 2019, **31**, 1807166.

34 G. Wang, J. Chen, Y. Ding, P. Cai, L. Yi, Y. Li, C. Tu, Y. Hou, Z. Wen and L. Dai, *Chem. Soc. Rev.*, 2021, **50**, 4993–5061.

35 S. X. Dou, W.-H. Lai and C. Cook, *Natl. Sci. Rev.*, 2023, **10**, nwad223.

36 Y. Wu, Z. Jiang, X. Lu, Y. Liang and H. Wang, *Nature*, 2019, **575**, 639–642.

37 S. Shen, X. Peng, L. Song, Y. Qiu, C. Li, L. Zhuo, J. He, J. Ren, X. Liu and J. Luo, *Small*, 2019, **15**, 1902229.

38 C.-T. Dinh, T. Burdyny, M. G. Kibria, A. Seifitokaldani, C. M. Gabardo, F. P. García de Arquer, A. Kiani, J. P. Edwards, P. De Luna, O. S. Bushuyev, C. Zou, R. Quintero-Bermudez, Y. Pang, D. Sinton and E. H. Sargent, *Science*, 2018, **360**, 783–787.

39 Y. Hori, K. Kikuchi and S. Suzuki, *Chem. Lett.*, 1985, **14**, 1695–1698.

40 J. Albero and H. García, in *Heterogeneous Photocatalysis: from Fundamentals to Green Applications*, ed. J. C. Colmenares and Y.-J. Xu, Springer Berlin Heidelberg, Berlin, Heidelberg, 2016, pp. 1–31, DOI: 10.1007/978-3-662-48719-8_1.

11874 | *J. Mater. Chem. A*, 2026, **14**, 11848–11879

This journal is © The Royal Society of Chemistry 2026

41 Z. Yin, G. T. R. Palmore and S. Sun, *Trends Chem.*, 2019, **1**, 739–750.

42 J. Huang and R. Buonsanti, *Chem. Mater.*, 2019, **31**, 13–25.

43 D. D. Zhu, J. L. Liu and S. Z. Qiao, *Adv. Mater.*, 2016, **28**, 3423–3452.

44 B. Cao, F.-Z. Li and J. Gu, *ACS Catal.*, 2022, **12**, 9735–9752.

45 W. Zhu, R. Michalsky, Ö. Metin, H. Lv, S. Guo, C. J. Wright, X. Sun, A. A. Peterson and S. Sun, *J. Am. Chem. Soc.*, 2013, **135**, 16833–16836.

46 X. Wang, J. F. de Araújo, W. Ju, A. Bagger, H. Schmies, S. Kühl, J. Rossmeisl and P. Strasser, *Nat. Nanotechnol.*, 2019, **14**, 1063–1070.

47 L. Jin, B. Liu, P. Wang, H. Yao, L. A. Achola, P. Kerns, A. Lopes, Y. Yang, J. Ho, A. Moewes, Y. Pei and J. He, *Nanoscale*, 2018, **10**, 14678–14686.

48 Y. Chen, C. W. Li and M. W. Kanan, *J. Am. Chem. Soc.*, 2012, **134**, 19969–19972.

49 S. Zhao, R. Jin and R. Jin, *ACS Energy Lett.*, 2018, **3**, 452–462.

50 J. A. Trindell, J. Clausmeyer and R. M. Crooks, *J. Am. Chem. Soc.*, 2017, **139**, 16161–16167.

51 L. Zhang, W. Wang, D. Jiang, E. Gao and S. Sun, *Nano Res.*, 2015, **8**, 821–831.

52 Z. Zhang, M. Chi, G. M. Veith, P. Zhang, D. A. Lutterman, J. Rosenthal, S. H. Overbury, S. Dai and H. Zhu, *ACS Catal.*, 2016, **6**, 6255–6264.

53 C. Cui, J. Han, X. Zhu, X. Liu, H. Wang, D. Mei and Q. Ge, *J. Catal.*, 2016, **343**, 257–265.

54 X. Zheng, P. De Luna, F. P. García de Arquer, B. Zhang, N. Becknell, M. B. Ross, Y. Li, M. N. Banis, Y. Li, M. Liu, O. Voznyy, C. T. Dinh, T. Zhuang, P. Stadler, Y. Cui, X. Du, P. Yang and E. H. Sargent, *Joule*, 2017, **1**, 794–805.

55 T. Zheng, K. Jiang and H. Wang, *Adv. Mater.*, 2018, **30**, 1802066.

56 A. Betts, V. Briega-Martos, A. Cuesta and E. Herrero, *ACS Catal.*, 2020, **10**, 8120–8130.

57 C. W. Li, J. Ciston and M. W. Kanan, *Nature*, 2014, **508**, 504–507.

58 H. Xie, T. Wang, J. Liang, Q. Li and S. Sun, *Nano Today*, 2018, **21**, 41–54.

59 X. Qin, T. Vegge and H. A. Hansen, *J. Am. Chem. Soc.*, 2023, **145**, 1897–1905.

60 J. Li, Y. Kuang, Y. Meng, X. Tian, W.-H. Hung, X. Zhang, A. Li, M. Xu, W. Zhou, C.-S. Ku, C.-Y. Chiang, G. Zhu, J. Guo, X. Sun and H. Dai, *J. Am. Chem. Soc.*, 2020, **142**, 7276–7282.

61 M. Khalil, G. T. M. Kadja, F. A. A. Nugroho, L. G. Sutanto, P. K. Jiwanti, F. F. Abdi, F. Hussin and M. K. Aroua, *Renew. Sustain. Energy Rev.*, 2024, **206**, 114869.

62 S. Yu, S. Louisia and P. Yang, *JACS Au*, 2022, **2**, 562–572.

63 K. Rossi and R. Buonsanti, *Acc. Chem. Res.*, 2022, **55**, 629–637.

64 H. S. Jeon, J. Timoshenko, F. Scholten, I. Sinev, A. Herzog, F. T. Haase and B. Roldan Cuenya, *J. Am. Chem. Soc.*, 2019, **141**, 19879–19887.

65 C. Kim, F. Dionigi, V. Beermann, X. Wang, T. Möller and P. Strasser, *Adv. Mater.*, 2019, **31**, 1805617.

66 Y. Kang, S. M. João, R. Lin, K. Liu, L. Zhu, J. Fu, W.-C. Cheong, S. Lee, K. Frank, B. Nickel, M. Liu, J. Lischner and E. Cortés, *Nat. Commun.*, 2024, **15**, 3923.

67 G. L. De Gregorio, T. Burdyny, A. Loiudice, P. Iyengar, W. A. Smith and R. Buonsanti, *ACS Catal.*, 2020, **10**, 4854–4862.

68 K. Manthiram, B. J. Beberwyck and A. P. Alivisatos, *J. Am. Chem. Soc.*, 2014, **136**, 13319–13325.

69 Y. Li, D. Kim, S. Louisia, C. Xie, Q. Kong, S. Yu, T. Lin, S. Aloni, S. C. Fakra and P. Yang, *Proc. Natl. Acad. Sci. U. S. A.*, 2020, **117**, 9194–9201.

70 S. Popović, M. Smiljanić, P. Jovanovič, J. Vavra, R. Buonsanti and N. Hodnik, *Angew. Chem., Int. Ed.*, 2020, **59**, 14736–14746.

71 J. A. Lopez-Sanchez, N. Dimitratos, C. Hammond, G. L. Brett, L. Kesavan, S. White, P. Miedziak, R. Tiruvalam, R. L. Jenkins, A. F. Carley, D. Knight, C. J. Kiely and G. J. Hutchings, *Nat. Chem.*, 2011, **3**, 551–556.

72 Z. Niu and Y. Li, *Chem. Mater.*, 2014, **26**, 72–83.

73 D. Li, C. Wang, D. Tripkovic, S. Sun, N. M. Markovic and V. R. Stamenkovic, *ACS Catal.*, 2012, **2**, 1358–1362.

74 F. Li and Q. Tang, *J. Mater. Chem. A*, 2019, **7**, 19872–19880.

75 T. Zhang, J. He and X. Xiang, *ChemCatChem*, 2023, **15**, e202301119.

76 Q. Zhu, C. J. Murphy and L. R. Baker, *J. Am. Chem. Soc.*, 2022, **144**, 2829–2840.

77 X. Kong, J. Zhu, Z. Xu and Z. Geng, *Angew. Chem., Int. Ed.*, 2025, **64**, e202417562.

78 X. Wei, Z. Yin, K. Lyu, Z. Li, J. Gong, G. Wang, L. Xiao, J. Lu and L. Zhuang, *ACS Catal.*, 2020, **10**, 4103–4111.

79 Y. Ma, J. Wang, J. Yu, J. Zhou, X. Zhou, H. Li, Z. He, H. Long, Y. Wang, P. Lu, J. Yin, H. Sun, Z. Zhang and Z. Fan, *Matter*, 2021, **4**, 888–926.

80 J. Li, F. He, Z. Cheng, J. Chen, X. Zhang and Z. Qi, *J. Mater. Chem. A*, 2025, **13**, 12039–12056.

81 Q. Fan, G. Bao, X. Chen, Y. Meng, S. Zhang and X. Ma, *ACS Catal.*, 2022, **12**, 7517–7523.

82 M. Wan, Z. Yang, H. Morgan, J. Shi, F. Shi, M. Liu, H.-W. Wong, Z. Gu and F. Che, *J. Am. Chem. Soc.*, 2023, **145**, 26038–26051.

83 N. A. Nosratabad, Z. Jin, L. Du, M. Thakur and H. Mattoussi, *Chem. Mater.*, 2021, **33**, 921–933.

84 N. Arabzadeh Nosratabad, Z. Jin, H. Arabzadeh, B. Chen, C. Huang and H. Mattoussi, *Dalton Trans.*, 2024, **53**, 467–483.

85 L. Zhang, Z. Wei, S. Thanneeru, M. Meng, M. Kruzyk, G. Ung, B. Liu and J. He, *Angew. Chem., Int. Ed.*, 2019, **58**, 15834–15840.

86 Q. Luo, J. A. Adewuyi, L. Smith, F. K. Masese, Y. Chen, R. M. Kasi, A. D. Aderibigbe, S. Sun, G. Ung and J. He, *ACS Appl. Mater. Interfaces*, 2025, **17**, 43899–43908.

87 J. R. Pankhurst, Y. T. Guntern, M. Mensi and R. Buonsanti, *Chem. Sci.*, 2019, **10**, 10356–10365.

88 Z. Han, X. Wang, Z. Li, J. Gao, Z. Hu, Y. Wang, S. Li, X. Mao, Q.-h. Yang and Z. Weng, *Angew. Chem., Int. Ed.*, 2025, **64**, e202504785.

This journal is © The Royal Society of Chemistry 2026

J. Mater. Chem. A, 2026, **14**, 1848–1879 | **11875**

89 J. Chen, L. Fan, Y. Zhao, H. Yang, D. Wang, B. Hu, S. Xi and L. Wang, *Chem. Commun.*, 2024, **60**, 3178–3181.

90 K. S. Rawat, A. Mahata, I. Choudhuri and B. Pathak, *J. Phys. Chem. C*, 2016, **120**, 8821–8831.

91 S. Sung, X. Li, L. M. Wolf, J. R. Meeder, N. S. Bhuvanesh, K. A. Grice, J. A. Panetier and M. Nippe, *J. Am. Chem. Soc.*, 2019, **141**, 6569–6582.

92 J.-J. Lv, R. Yin, L. Zhou, J. Li, R. Kikas, T. Xu, Z.-J. Wang, H. Jin, X. Wang and S. Wang, *Angew. Chem., Int. Ed.*, 2022, **61**, e202207252.

93 Z. Xing, L. Hu, D. S. Ripatti, X. Hu and X. Feng, *Nat. Commun.*, 2021, **12**, 136.

94 Y. C. Tan, K. B. Lee, H. Song and J. Oh, *Joule*, 2020, **4**, 1104–1120.

95 A. Thevenon, A. Rosas-Hernández, A. M. Fontani Herreros, T. Agapie and J. C. Peters, *ACS Catal.*, 2021, **11**, 4530–4537.

96 Y. Lin, T. Wang, L. Zhang, G. Zhang, L. Li, Q. Chang, Z. Pang, H. Gao, K. Huang, P. Zhang, Z.-J. Zhao, C. Pei and J. Gong, *Nat. Commun.*, 2023, **14**, 3575.

97 E. Shirzadi, Q. Jin, A. S. Zeraati, R. Dorakhan, T. J. Goncalves, J. Abed, B.-H. Lee, A. S. Rasouli, J. Wicks, J. Zhang, P. Ou, V. Boureau, S. Park, W. Ni, G. Lee, C. Tian, D. M. Meira, D. Sinton, S. Siahrostami and E. H. Sargent, *Nat. Commun.*, 2024, **15**, 2995.

98 M. Sun, J. Cheng and M. Yamauchi, *Nat. Commun.*, 2024, **15**, 491.

99 Z.-Z. Niu, F.-Y. Gao, X.-L. Zhang, P.-P. Yang, R. Liu, L.-P. Chi, Z.-Z. Wu, S. Qin, X. Yu and M.-R. Gao, *J. Am. Chem. Soc.*, 2021, **143**, 8011–8021.

100 M. Fang, M. Wang, Z. Wang, Z. Zhang, H. Zhou, L. Dai, Y. Zhu and L. Jiang, *J. Am. Chem. Soc.*, 2023, **145**, 11323–11332.

101 M. Fan, J. E. Huang, R. K. Miao, Y. Mao, P. Ou, F. Li, X.-Y. Li, Y. Cao, Z. Zhang, J. Zhang, Y. Yan, A. Ozden, W. Ni, Y. Wang, Y. Zhao, Z. Chen, B. Khatir, C. P. O'Brien, Y. Xu, Y. C. Xiao, G. I. N. Waterhouse, K. Golovin, Z. Wang, E. H. Sargent and D. Sinton, *Nat. Catal.*, 2023, **6**, 763–772.

102 M. D. Porter, T. B. Bright, D. L. Allara and C. E. Chidsey, *J. Am. Chem. Soc.*, 1987, **109**, 3559–3568.

103 H. Finklea, L. Robinson, A. Blackburn, B. Richter, D. Allara and T. Bright, *Langmuir*, 1986, **2**, 239–244.

104 E. Boubour and R. B. Lennox, *Langmuir*, 2000, **16**, 4222–4228.

105 R. Haag, M. A. Rampi, R. E. Holmlin and G. M. Whitesides, *J. Am. Chem. Soc.*, 1999, **121**, 7895–7906.

106 P. Fenter, A. Eberhardt and P. Eisenberger, *Science*, 1994, **266**, 1216–1218.

107 J. Aizenberg, A. J. Black and G. M. Whitesides, *Nature*, 1999, **398**, 495–498.

108 S. Chen and R. W. Murray, *Langmuir*, 1999, **15**, 682–689.

109 C. Yi, Y. Yang, B. Liu, J. He and Z. Nie, *Chem. Soc. Rev.*, 2020, **49**, 465–508.

110 L. Michalek, L. Barner and C. Barner-Kowollik, *Adv. Mater.*, 2018, **30**, 1706321.

111 Q. Luo, H. Duan, M. C. McLaughlin, K. Wei, J. Tapia, J. A. Adewuyi, S. Shuster, M. Liaqat, S. L. Suib, G. Ung, P. Bai, S. Sun and J. He, *Chem. Sci.*, 2023, **14**, 9664–9677.

112 Y. Chae, H. Kim, D. K. Lee, U. Lee and D. H. Won, *Nano Energy*, 2024, **130**, 110134.

113 P. Chinwangso, H. J. Lee, A. C. Jamison, M. D. Marquez, C. S. Park and T. R. Lee, *Langmuir*, 2017, **33**, 1751–1762.

114 Y.-S. Shon, S. Lee, R. Colorado, S. S. Perry and T. R. Lee, *J. Am. Chem. Soc.*, 2000, **122**, 7556–7563.

115 G. M. Whitesides and P. E. J. L. Laibinis, *Langmuir*, 1990, **6**, 87–96.

116 D. Wakerley, S. Lamaison, F. Ozanam, N. Menguy, D. Mercier, P. Marcus, M. Fontecave and V. Mougel, *Nat. Mater.*, 2019, **18**, 1222–1227.

117 M. W. J. Beulen, M. I. Kastenberg, F. C. J. M. van Veggel and D. N. Reinhoudt, *Langmuir*, 1998, **14**, 7463–7467.

118 N. C. Ramos, J. W. Medlin and A. Holewinski, *ACS Appl. Mater. Interfaces*, 2023, **15**, 14470–14480.

119 H.-Q. Liang, S. Zhao, X.-M. Hu, M. Ceccato, T. Skrydstrup and K. Daasbjerg, *ACS Catal.*, 2021, **11**, 958–966.

120 J. H. Lee, S. Kattel, Z. Xie, B. M. Tackett, J. Wang, C.-J. Liu and J. G. Chen, *Adv. Funct. Mater.*, 2018, **28**, 1804762.

121 J. Pellessier, X. Gong, B. Li, J. Zhang, Y. Gang, K. Hambleton, C. Podder, Z. Gao, H. Zhou, G. Wang, H. Pan and Y. Li, *J. Mater. Chem. A*, 2023, **11**, 26252–26264.

122 L. Li, J. Chen, V. S. S. Mosali, Y. Liang, A. M. Bond, Q. Gu and J. Zhang, *Angew. Chem., Int. Ed.*, 2022, **61**, e202208534.

123 M. N. Hopkinson, C. Richter, M. Schedler and F. Glorius, *Nature*, 2014, **510**, 485–496.

124 B. Qie, Z. Wang, J. Jiang, Z. Zhang, P. H. Jacobse, J. Lu, X. Li, F. Liu, A. N. Alexandrova, S. G. Louie, M. F. Crommie and F. R. Fischer, *Science*, 2024, **384**, 895–901.

125 K. C. Edwards, M. Vasiliu, J. W. Maxwell, C. E. Castillo, D. M. Marion, R. Craciun, J. F. Hall, D. Tapu and D. A. Dixon, *J. Phys. Chem. A*, 2023, **127**, 10838–10850.

126 L. Zhang, Z. Wei, M. Meng, G. Ung and J. He, *J. Mater. Chem. A*, 2020, **8**, 15900–15908.

127 S. Thanneeru, K. M. Ayers, M. Anuganti, L. Zhang, C. V. Kumar, G. Ung and J. He, *J. Mater. Chem. C*, 2020, **8**, 2280–2288.

128 Z. Wei, M. Kayceety, A. Price, K. Wei, Q. Luo, S. Thanneeru, S. Sun and J. He, *ACS Appl. Mater. Interfaces*, 2022, **14**, 55227–55237.

129 H. Duan, Y. Lin and J. He, in *World Scientific Reference on Plasmonic Nanomaterials*, World Scientific, 2021, vol. 22, pp. 409–432.

130 Y. Chen, K. Wei, H. Duan, H. Sun, Z. Yu, A. Zohaib, P. Zhu, J. He and S. Sun, *J. Am. Chem. Soc.*, 2025, **147**, 14845–14855.

131 N. Kumar, J. He and J. F. Rusling, *Chem. Soc. Rev.*, 2023, **52**, 5135–5171.

132 T. H. M. Pham, J. Zhang, M. Li, T.-H. Shen, Y. Ko, V. Tileli, W. Luo and A. Züttel, *Adv. Energy Mater.*, 2022, **12**, 2103663.

133 Y. Li, Z. Pei, D. Luan and X. W. Lou, *Angew. Chem., Int. Ed.*, 2023, **62**, e202302128.

134 S. Jia, Q. Zhu, M. Chu, S. Han, R. Feng, J. Zhai, W. Xia, M. He, H. Wu and B. Han, *Angew. Chem., Int. Ed.*, 2021, **60**, 10977–10982.

135 L. Su, Q. Hua, G. Feng, Y. Yang, H. Mei, Y. Yu, X. Chang and Z. Huang, *Adv. Funct. Mater.*, 2025, **35**, 2425636.

11876 | *J. Mater. Chem. A*, 2026, **14**, 11848–11879

This journal is © The Royal Society of Chemistry 2026

136 X. Fan, W. Nie, H. Tsai, N. Wang, H. Huang, Y. Cheng, R. Wen, L. Ma, F. Yan and Y. Xia, *Adv. Sci.*, 2019, **6**, 1900813.

137 M. Vosgueritchian, D. J. Lipomi and Z. Bao, *Adv. Funct. Mater.*, 2012, **22**, 421–428.

138 H. Huang, Y. Zhao, T. Cong, C. Li, N. Wen, X. Zuo, Y. Guo, H. Zhang, Z. Fan and L. Pan, *Adv. Funct. Mater.*, 2022, **32**, 2110777.

139 X. Chen, S. Jia, C. Chen, J. Jiao, J. Zhai, T. Deng, C. Xue, H. Cheng, M. Dong, W. Xia, J. Zeng, X. Xing, H. Wu, M. He and B. Han, *Adv. Mater.*, 2024, **36**, 2310273.

140 J. Cheng, L. Chen, X. Xie, K. Feng, H. Sun, Y. Qin, W. Hua, Z. Zheng, Y. He, W. Pan, W. Yang, F. Lyu, J. Zhong, Z. Deng, Y. Jiao and Y. Peng, *Angew. Chem., Int. Ed.*, 2023, **62**, e202312113.

141 G. Li, L. Huang, C. Wei, H. Shen, Y. Liu, Q. Zhang, J. Su, Y. Song, W. Guo, X. Cao, B. Z. Tang, M. Robert and R. Ye, *Angew. Chem., Int. Ed.*, 2024, **63**, e202400414.

142 C. Kim, J. C. Bui, X. Luo, J. K. Cooper, A. Kusoglu, A. Z. Weber and A. T. Bell, *Nat. Energy*, 2021, **6**, 1026–1034.

143 M. L. J. Peerlings, M. E. T. Vink-van Ittersum, J. W. de Rijk, P. E. de Jongh and P. Ngene, *ACS Catal.*, 2025, **15**, 9695–9705.

144 C. Yu, T. Lei, L. Xu, C. Jin, J. Yi, S. Liu, S. Lin, Y. Yang, H. Song, K. Wang, H. Fan, C. Zheng, X. Zhang and X. Gao, *J. Mater. Chem. A*, 2024, **12**, 17181–17192.

145 F. P. García de Arquer, C.-T. Dinh, A. Ozden, J. Wicks, C. McCallum, A. R. Kirmani, D.-H. Nam, C. Gabardo, A. Seifitokaldani, X. Wang, Y. C. Li, F. Li, J. Edwards, L. J. Richter, S. J. Thorpe, D. Sinton and E. H. Sargent, *Science*, 2020, **367**, 661–666.

146 P. Papangelakis, R. K. Miao, R. Lu, H. Liu, X. Wang, A. Ozden, S. Liu, N. Sun, C. P. O'Brien, Y. Hu, M. Shakouri, Q. Xiao, M. Li, B. Khatir, J. E. Huang, Y. Wang, Y. C. Xiao, F. Li, A. S. Zeraati, Q. Zhang, P. Liu, K. Golovin, J. Y. Howe, H. Liang, Z. Wang, J. Li, E. H. Sargent and D. Sinton, *Nat. Energy*, 2024, **9**, 1011–1020.

147 J. Sun, B. Wu, Z. Wang, H. Guo, G. Yan, H. Duan, G. Li, Y. Wang and J. Wang, *Energy Environ. Sci.*, 2025, **18**, 1027–1037.

148 J. Park, Y. Chae, C. Lee, G. Kwon, W. H. Lee, H. S. Jeon, J. Cho, D. H. Won and J. H. Koh, *ACS Catal.*, 2025, **15**, 12222–12230.

149 Y. I. Song, B. Yoon, C. Lee, D. Kim, M. H. Han, H. Han, W. H. Lee, D. H. Won, J. K. Kim, H. S. Jeon and J. H. Koh, *Adv. Sci.*, 2024, **11**, 2406281.

150 X. Ye, C. Zheng, J. Chen, Y. Gao and C. B. Murray, *Nano Lett.*, 2013, **13**, 765–771.

151 J. Mosquera, D. Wang, S. Bals and L. M. Liz-Marzán, *Acc. Chem. Res.*, 2023, **56**, 1204–1212.

152 C. J. Murphy, T. K. Sau, A. M. Gole, C. J. Orendorff, J. Gao, L. Gou, S. E. Hunyadi and T. Li, *J. Phys. Chem. B*, 2005, **109**, 13857–13870.

153 D. Muhuri, M. Sarkar, H. Duan, L. A. Hanson and J. He, *Angew. Chem., Int. Ed.*, 2025, **64**, e202516071.

154 L. Xue, Z. Gao, T. Ning, W. Li, J. Li, J. Yin, L. Xiao, G. Wang and L. Zhuang, *Angew. Chem., Int. Ed.*, 2023, **62**, e202309519.

155 X. Chen, J. Chen, N. M. Alghoraibi, D. A. Henckel, R. Zhang, U. O. Nwabara, K. E. Madsen, P. J. A. Kenis, S. C. Zimmerman and A. A. Gewirth, *Nat. Catal.*, 2021, **4**, 20–27.

156 Q. Luo, J. Tapia, L. Zhou, C.-H. Liu, M. Liaqat, H. Duan, Z. Yang, M.-P. Nieh, T. Emrick, P. Bai and J. He, *Nanoscale*, 2024, **16**, 15558–15567.

157 H.-G. Qin, Y.-F. Du, Y.-Y. Bai, F.-Z. Li, X. Yue, H. Wang, J.-Z. Peng and J. Gu, *Nat. Commun.*, 2023, **14**, 5640.

158 X.-Q. Li, G.-Y. Duan, J.-W. Chen, L.-J. Han, S.-J. Zhang and B.-H. Xu, *Appl. Catal., B*, 2021, **297**, 120471.

159 G.-Y. Duan, X.-Q. Li, G.-R. Ding, L.-J. Han, B.-H. Xu and S.-J. Zhang, *Angew. Chem., Int. Ed.*, 2022, **61**, e202110657.

160 A. H. Mamaghani, J. Liu, Z. Zhang, R. Gao, Y. Wu, H. Li, M. Feng and Z. Chen, *Adv. Energy Mater.*, 2024, **14**, 2402278.

161 M. Ding, R. W. Flaig, H.-L. Jiang and O. M. Yaghi, *Chem. Soc. Rev.*, 2019, **48**, 2783–2828.

162 C. S. Diercks, Y. Liu, K. E. Cordova and O. M. Yaghi, *Nat. Mater.*, 2018, **17**, 301–307.

163 D.-H. Nam, O. Shekhah, A. Ozden, C. McCallum, F. Li, X. Wang, Y. Lum, T. Lee, J. Li, J. Wicks, A. Johnston, D. Sinton, M. Eddaoudi and E. H. Sargent, *Adv. Mater.*, 2022, **34**, 2207088.

164 R. Freund, O. Zaremba, G. Arnauts, R. Ameloot, G. Skorupskii, M. Dincă, A. Bavykina, J. Gascon, A. Ejsmont, J. Goscianska, M. Kalmutzki, U. Lächelt, E. Ploetz, C. S. Diercks and S. Wuttke, *Angew. Chem., Int. Ed.*, 2021, **60**, 23975–24001.

165 D.-H. Yang, Y. Tao, X. Ding and B.-H. Han, *Chem. Soc. Rev.*, 2022, **51**, 761–791.

166 S. Zheng, S. Xia, Z. Ouyang, S. Bi, Y. Fu, G. Liu, Y. Wang, Q. Xu and G. Zeng, *ACS Catal.*, 2024, **14**, 18524–18534.

167 Y. Zhao, L. Zheng, D. Jiang, W. Xia, X. Xu, Y. Yamauchi, J. Ge and J. Tang, *Small*, 2021, **17**, 2006590.

168 J. Yuan, S. Chen, Y. Zhang, R. Li, J. Zhang and T. Peng, *Adv. Mater.*, 2022, **34**, 2203139.

169 M. Xu, C. Lai, X. Liu, B. Li, M. Zhang, F. Xu, S. Liu, L. Li, L. Qin, H. Yi and Y. Fu, *J. Mater. Chem. A*, 2021, **9**, 24148–24174.

170 L. Ma, W. Hu, B. Mei, H. Liu, B. Yuan, J. Zang, T. Chen, L. Zou, Z. Zou, B. Yang, Y. Yu, J. Ma, Z. Jiang, K. Wen and H. Yang, *ACS Catal.*, 2020, **10**, 4534–4542.

171 Y. Zou and S. Wang, *Adv. Sci.*, 2021, **8**, 2003579.

172 B. Peng, H. She, Z. Wei, Z. Sun, Z. Deng, Z. Sun and W. Chen, *Nat. Commun.*, 2025, **16**, 2217.

173 D.-H. Nam, O. Shekhah, G. Lee, A. Mallick, H. Jiang, F. Li, B. Chen, J. Wicks, M. Eddaoudi and E. H. Sargent, *J. Am. Chem. Soc.*, 2020, **142**, 21513–21521.

174 Y.-R. Wang, H.-M. Ding, X.-Y. Ma, M. Liu, Y.-L. Yang, Y. Chen, S.-L. Li and Y.-Q. Lan, *Angew. Chem., Int. Ed.*, 2022, **61**, e202114648.

175 C. Li, W. Ju, S. Vijay, J. Timoshenko, K. Mou, D. A. Cullen, J. Yang, X. Wang, P. Pachfule and S. J. A. C. Brückner, *Angew. Chem., Int. Ed.*, 2022, **134**, e202114707.

This journal is © The Royal Society of Chemistry 2026

J. Mater. Chem. A, 2026, **14**, 11848–11879 | **11877**

176 H. Zhong, M. Ghorbani-Asl, K. H. Ly, J. Zhang, J. Ge, M. Wang, Z. Liao, D. Makarov, E. Zschech, E. Brunner, I. M. Weidinger, J. Zhang, A. V. Krasheninnikov, S. Kaskel, R. Dong and X. Feng, *Nat. Commun.*, 2020, **11**, 1409.

177 S. Mukhopadhyay, R. Shimoni, I. Liberman, R. Ifraemov, I. Rozenberg and I. Hod, *Angew. Chem., Int. Ed.*, 2021, **60**, 13423–13429.

178 S. Mukhopadhyay, M. S. Naeem, G. Shiva Shanker, A. Ghatak, A. R. Kottaichamy, R. Shimoni, L. Avram, I. Liberman, R. Balilty, R. Ifraemov, I. Rozenberg, M. Shalom, N. López and I. Hod, *Nat. Commun.*, 2024, **15**, 3397.

179 Q. Yang, Q. Xu and H.-L. Jiang, *Chem. Soc. Rev.*, 2017, **46**, 4774–4808.

180 Q.-L. Zhu, J. Li and Q. Xu, *J. Am. Chem. Soc.*, 2013, **135**, 10210–10213.

181 G. Lu, S. Li, Z. Guo, O. K. Farha, B. G. Hauser, X. Qi, Y. Wang, X. Wang, S. Han, X. Liu, J. S. DuChene, H. Zhang, Q. Zhang, X. Chen, J. Ma, S. C. J. Loo, W. D. Wei, Y. Yang, J. T. Hupp and F. Huo, *Nat. Chem.*, 2012, **4**, 310–316.

182 C.-H. Kuo, Y. Tang, L.-Y. Chou, B. T. Sneed, C. N. Brodsky, Z. Zhao and C.-K. Tsung, *J. Am. Chem. Soc.*, 2012, **134**, 14345–14348.

183 M. Zhao, K. Yuan, Y. Wang, G. Li, J. Guo, L. Gu, W. Hu, H. Zhao and Z. Tang, *Nature*, 2016, **539**, 76–80.

184 T. Yan, P. Wang and W.-Y. Sun, *Small*, 2023, **19**, 2206070.

185 N. Zhang and Y. Zhang, *Chem. Eng. J.*, 2024, **499**, 156694.

186 Y. Zhang, Y. Chen, X. Wang, Y. Feng, H. Zhang and G. Zhang, *Angew. Chem., Int. Ed.*, 2023, **62**, e202302241.

187 A. Singh, S. Barman, F. A. Rahimi, A. Dey, R. Jena, R. Kumar, N. Mathew, D. Bhattacharyya and T. K. Maji, *Energy Environ. Sci.*, 2024, **17**, 2315–2325.

188 S. Chen, W.-H. Li, W. Jiang, J. Yang, J. Zhu, L. Wang, H. Ou, Z. Zhuang, M. Chen, X. Sun, D. Wang and Y. Li, *Angew. Chem., Int. Ed.*, 2022, **61**, e202114450.

189 C. He, D.-H. Si, L. Han, Z.-N. Xu, Z. Chen, R. Cao and Y.-B. Huang, *ACS Catal.*, 2024, **14**, 3943–3954.

190 J.-D. Yi, R. Xie, Z.-L. Xie, G.-L. Chai, T.-F. Liu, R.-P. Chen, Y.-B. Huang and R. Cao, *Angew. Chem., Int. Ed.*, 2020, **59**, 23641–23648.

191 Z.-H. Zhao, K. Zheng, N.-Y. Huang, H.-L. Zhu, J.-R. Huang, P.-Q. Liao and X.-M. Chen, *Chem. Commun.*, 2021, **57**, 12764–12767.

192 X. Min and M. W. Kanan, *J. Am. Chem. Soc.*, 2015, **137**, 4701–4708.

193 S. Lin, C. S. Diercks, Y.-B. Zhang, N. Kornienko, E. M. Nichols, Y. Zhao, A. R. Paris, D. Kim, P. Yang, O. M. Yaghi and C. J. Chang, *Science*, 2015, **349**, 1208–1213.

194 M. Lu, M. Zhang, J. Liu, Y. Chen, J.-P. Liao, M.-Y. Yang, Y.-P. Cai, S.-L. Li and Y.-Q. Lan, *Angew. Chem., Int. Ed.*, 2022, **61**, e202200003.

195 M. Zhang, M. Lu, M.-Y. Yang, J.-P. Liao, Y.-F. Liu, H.-J. Yan, J.-N. Chang, T.-Y. Yu, S.-L. Li and Y.-Q. Lan, *eScience*, 2023, **3**, 100116.

196 A. Ozden, J. Li, S. Kandambeth, X.-Y. Li, S. Liu, O. Shekhah, P. Ou, Y. Zou Finfrock, Y.-K. Wang, T. Alkayyali, F. Pelayo García de Arquer, V. S. Kale, P. M. Bhatt, A. H. Ip, M. Eddaoudi, E. H. Sargent and D. Sinton, *Nat. Energy*, 2023, **8**, 179–190.

197 Q. Zhao, Y. Wang, M. Li, S. Zhu, T. Li, J. Yang, T. Lin, E. P. Delmo, Y. Wang, J. Jang, M. Gu and M. Shao, *SmartMat*, 2022, **3**, 183–193.

198 S. Zheng, D.-H. Si, H. Guo, Q.-J. Wu, H.-J. Zhu, Y.-B. Huang and R. Cao, *ACS Nano*, 2025, **19**, 24130–24139.

199 S. Cai, S. Tao, M. Chong, Z. Shi, X. Liu, D. Cheng and F. Chen, *ACS Appl. Mater. Interfaces*, 2024, **16**, 55267–55275.

200 Y.-M. Wang, F.-Q. Yan, Q.-Y. Wang, C.-X. Du, L.-Y. Wang, B. Li, S. Wang and S.-Q. Zang, *Nat. Commun.*, 2024, **15**, 1843.

201 C. Li, Y. Wang, C. Wang, Q. Wu, X. Lv, S. Xie, L. Kong, J. Feng, Z. Li, A.-J. Wang, J. Kang and F. Yang, *ACS Appl. Mater. Interfaces*, 2025, **17**, 26594–26603.

202 Y. Kong, B. Lyu, C. Fan, Y. Yang, X. Wang, B. Shi, J. Jiang, H. Wu and Z. Jiang, *J. Am. Chem. Soc.*, 2023, **145**, 27984–27992.

203 Z. Zhu, Y. Zhu, Z. Ren, D. Liu, F. Yue, D. Sheng, P. Shao, X. Huang, X. Feng, A.-X. Yin, J. Xie and B. Wang, *J. Am. Chem. Soc.*, 2024, **146**, 1572–1579.

204 Z. Qian, Y. Liu, Z. Lin, N. Ye, Y. Tan, F. Liu, Y. Gu, Q. Huang, H. Guo, M. Luo and S. Guo, *J. Am. Chem. Soc.*, 2025, **147**, 21877–21884.

205 M. Fang, X. Miao, Z. Huang, M. Wang, X. Feng, Z. Wang, Y. Zhu, L. Dai and L. Jiang, *J. Am. Chem. Soc.*, 2024, **146**, 27060–27069.

206 J. Yu, C. Mu, B. Yan, X. Qin, C. Shen, H. Xue and H. Pang, *Mater. Horiz.*, 2017, **4**, 557–569.

207 M. Mukoyoshi and H. Kitagawa, *Chem. Commun.*, 2022, **58**, 10757–10767.

208 L.-X. Liu, C. Qin, T. Deng, L. Sun, Z. Chen and X. Han, *J. Mater. Chem. A*, 2024, **12**, 26421–26438.

209 C. A. Trickett, A. Helal, B. A. Al-Maythalony, Z. H. Yamani, K. E. Cordova and O. M. Yaghi, *Nat. Rev. Mater.*, 2017, **2**, 17045.

210 Q. Wang and D. Astruc, *Chem. Rev.*, 2020, **120**, 1438–1511.

211 Y. Zhang, X.-Y. Zhang and W.-Y. Sun, *ACS Catal.*, 2023, **13**, 1545–1553.

212 D.-H. Nam, O. S. Bushuyev, J. Li, P. De Luna, A. Seifitokaldani, C.-T. Dinh, F. P. García de Arquer, Y. Wang, Z. Liang, A. H. Proppe, C. S. Tan, P. Todorović, O. Shekhah, C. M. Gabardo, J. W. Jo, J. Choi, M.-J. Choi, S.-W. Baek, J. Kim, D. Sinton, S. O. Kelley, M. Eddaoudi and E. H. Sargent, *J. Am. Chem. Soc.*, 2018, **140**, 11378–11386.

213 X. Xie, X. Zhang, M. Xie, L. Xiong, H. Sun, Y. Lu, Q. Mu, M. H. Rummeli, J. Xu, S. Li, J. Zhong, Z. Deng, B. Ma, T. Cheng, W. A. Goddard and Y. Peng, *Nat. Commun.*, 2022, **13**, 63.

214 Y. Hori, H. Wakebe, T. Tsukamoto and O. Koga, *Surf. Sci.*, 1995, **335**, 258–263.

11878 | *J. Mater. Chem. A*, 2026, **14**, 11848–11879

This journal is © The Royal Society of Chemistry 2026

215 S. Mezzavilla, S. Horch, I. E. L. Stephens, B. Seger and I. Chorkendorff, *Angew. Chem., Int. Ed.*, 2019, **58**, 3774–3778.

216 A. Kim, C. Kim, T. Waltmann, T. Vo, E. M. Kim, J. Kim, Y.-T. Shao, A. Michelson, J. R. Crockett, F. C. Kalutantirige, E. Yang, L. Yao, C.-Y. Hwang, Y. Zhang, Y.-S. Liu, H. An, Z. Gao, J. Kim, S. Mandal, D. A. Muller, K. A. Fichthorn, S. C. Glotzer and Q. Chen, *Nature*, 2025, **646**, 592–600.

217 N. L. Dominique, A. Chandran, I. M. Jensen, D. M. Jenkins and J. P. Camden, *Chem.–Eur. J.*, 2024, **30**, e202303681.

218 D. Kim, S. Yu, F. Zheng, I. Roh, Y. Li, S. Louisia, Z. Qi, G. A. Somorjai, H. Frei, L.-W. Wang and P. Yang, *Nat. Energy*, 2020, **5**, 1032–1042.

219 H. Dridi, C. Comminges, C. Morais, J.-C. Meledje, K. B. Kokoh, C. Costentin and J.-M. Savéant, *J. Am. Chem. Soc.*, 2017, **139**, 13922–13928.

220 C. Costentin, J. C. Canales, B. Haddou and J.-M. Savéant, *J. Am. Chem. Soc.*, 2013, **135**, 17671–17674.

221 W. Xie, J. Xu, U. Md Idros, J. Katsuhira, M. Fuki, M. Hayashi, M. Yamanaka, Y. Kobori and R. Matsubara, *Nat. Chem.*, 2023, **15**, 794–802.

222 S. Thanneeru, J. K. Nganga, A. S. Amin, B. Liu, L. Jin, A. M. Angeles-Boza and J. He, *ChemCatChem*, 2017, **9**, 1157–1162.

223 W. W. Kramer and C. C. L. McCrory, *Chem. Sci.*, 2016, **7**, 2506–2515.

224 J. M. Vadillo, L. Gómez-Coma, A. Garea and A. Irabien, *Membranes*, 2020, **10**, 234.

This journal is © The Royal Society of Chemistry 2026

J. Mater. Chem. A, 2026, **14**, 11848–11879 | **11879**